

# **Towards a feed material adaptive optical belt sorter: A simulation study utilizing a DEM-CFD approach**

Albert Bauer<sup>1,\*</sup>, Georg Maier<sup>2</sup>, Marcel Reith-Braun<sup>3</sup>, Harald Kruggel-Emden<sup>1</sup>, Florian Pfaff<sup>3</sup>, Robin Gruna<sup>2</sup>, Uwe Hanebeck<sup>3</sup>, Thomas Längle<sup>2</sup>

<sup>1</sup>Technische Universität Berlin, Chair of Mechanical Process Engineering and Solids Processing, Ernst-Reuter-Platz 1, 10587 Berlin, Germany.

<sup>2</sup> Fraunhofer IOSB, Institute of Optronics, System Technologies and Image Exploitation, Fraunhoferstrasse 1, 76131 Karlsruhe, Germany

<sup>3</sup> Intelligent Sensor-Actuator-Systems Laboratory (ISAS), Karlsruhe Institute of Technology, 76131 Karlsruhe, Germany

Email corresponding author: a.bauer@tu-berlin.de

## **Abstract**

In this investigation, a DEM-CFD model of an optical belt sorter is modified to become adaptive to varying belt speeds. For that, the positions and orientations of the nozzle bar and collecting containers are rearranged. Also, the duration of nozzle activation and optimal position of particle ejection are adjusted. For the derivation of optimal velocity-dependent parameters, a two-dimensional model is derived and optimized as a pre-processing step. The derived parameters are applied to the three-dimensional DEM-CFD model. Two optically distinguishable types of demolition waste materials are considered. All conveyor belt velocities are investigated with instantaneously and lagged activated nozzles, which represent fast and realistic triggered nozzle activations. The application of optimized sorting setups shows promising sorting results for a broad range of conveyor belt velocities. The obtained results are discussed in terms of their feasibility in being applied to real optical belt sorters.

Keywords: Discrete Element Method (DEM), Computational Fluid Dynamics (CFD), Optical belt sorting, Sorting optimization

## 1 Introduction

Sensor-based sorters play an important role in material pre-treatment in the mining industry [1]–[3], in food processing [4]–[8] and in waste sorting [9]–[12]. The growing importance of sorting quality is the main driver in sorting system development today [13]. Increasing demand for resources, along with growing environmental awareness, contributes to that aim and pushes it in the vast field of waste recycling especially. The European Union aims to improve waste recycling and decrease waste landfilling in the next years [14]. To name two examples, with only roughly 46 % of demolition waste (2011, [15]) and 37 % of plastic waste in the EU being currently recycled (2021, [16]), there is still a great need for improvement in particular for development in terms of sensor-based sorting. In sensor-based sorting, properties of material classes are measured by a sensor, and those classes are separated based on their properties. Sensor types and, therefore, measured properties can be manifold, for example, [13] elemental composition measured by X-ray fluorescence, reflection or absorption of infrared light, radiation measured by near-infrared spectrometry or hull detection measured via laser triangulation. In the present study, we focus on a sorting system that captures the particle color using a camera in the visible wavelength range. The principle of such an optical belt sorter is shown in Fig. 1. Either a line-scan camera or an area-scan camera detects the position and color of transported particles. The images are transferred to a data processing unit that controls an array of nozzles and calculates the specific nozzle, nozzle activation time and duration based on the particle movement by means of a sorting model. An estimation of particle movement is necessary, since the particle movement is unknown between the camera and nozzle array (see Section 3.1.2 for details).

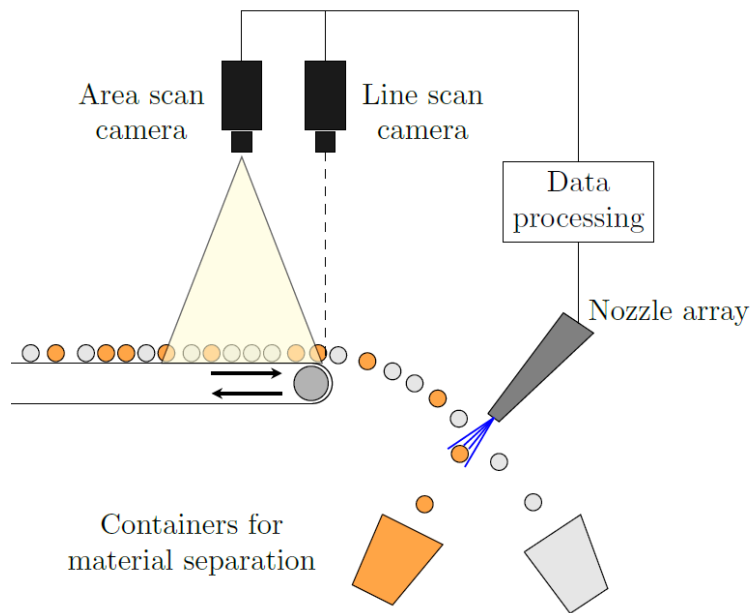


Fig. 1: Illustration of an optical belt sorter. Particles from different classes move on the conveyor belt and are either detected by a line-scan camera or an area-scan camera. Particle movement is tracked by the area-scan camera, or the position orthogonal to the movement is detected by the line-scan camera. The measurement data is then processed, and an activation signal is transmitted to the particular nozzle, which sorts out the reject material. The accept material can pass undisturbedly.

In sorting processes today, all components of the optical belt sorters are adjusted and fixed to the expected operational conditions, mainly mass flow and input composition. Those conditions, however, can fluctuate, possibly leading to reduced sorting accuracies. This behavior was recently shown in an experimental investigation by [15]. Such fluctuations are commonly being tried to be balanced by monitoring and pre-handling of material inflows. In [15], the authors used a hopper for the feed material to ensure that the material stream would remain constant and within the limit where the sorting performance is acceptable. Another approach, which we present in this work, is to directly react to the fluctuations within the sorter operation by adjusting the sorter hardware and parameters in an adequate way. As a result, operation points of the sorter can be found, at which the sorting accuracy remains constant or even increases, despite changing inflow conditions. This can be accomplished by influencing

the occupancy density on the conveyor belt through the conveyor belt velocity. The belt velocity affects the proximity of the particles on the belt, which could have a major impact on the sorting quality. This hypothesis is going to be investigated in this study.

The aim of our study can be summarized as follows: We want to develop an adaptive belt sorter that reacts to changed input feed conditions such as the mass flow rate by adapting the conveyor belt velocity, so that optimal sorting performance is assured. For that, we want to find a method to compute optimal sorting parameters at arbitrary belt velocities as a pre-processing step. With those parameters, we want to show that changing the conveyor belt velocities can be useful for improving the sorting accuracy. Our work can be seen as the first step towards an adaptive belt sorter, since conveyor belt velocity and sorting parameters are not changed during operation, but in advance.

To do so, a DEM-CFD model of an optical belt sorter, as depicted in Fig. 1, is utilized to identify the components and parameters that have to be adapted to changing conveyor belt velocities. These are the collecting containers' positions and orientations as well as nozzle activation time and nozzle activation offset. As a next step, a framework to compute optimal sorting parameters at arbitrary conveyor belt velocities is introduced. This is necessary for optimization since a direct optimization as part of the DEM-CFD would be too computationally costly. After the computation of the optimal parameters at a range of belt velocities, they are applied to the DEM-CFD model for validation. With those optimal parameters being validated, the sorting behavior of the optical belt sorter is investigated in detail for four inflow scenarios. Furthermore, the influence of the time lag between nozzle activation and actual formation of the air jet is analyzed in detail, since faster moving bulk particles require a faster sorting for proper material separation. A slow and thereby realistic sorting system is therefore compared to a fast-sorting system with no lag in terms of sorting accuracy. Sorting with the obtained parameters yields very good sorting results up to certain belt velocities. We can show that varying belt velocities can be beneficial for a range of sorting scenarios. The benefit is directly connected to the speed of nozzle activation.

For our study, we utilize the DEM-CFD method to model the whole sorting system. With the DEM, we compute the particle motion along with particle-particle and particle-wall interactions. The fluid phase is computed with a CFD simulation and coupled to the DEM at the area of the nozzles. We use unresolved DEM-CFD modeling, which means that the flow around the particles is not resolved in detail. The fluid force acting onto the particles is modeled by a drag force provided through a correlation instead. For material, we exemplarily consider two optically distinguishable rubble materials (brick and sand-lime brick) where the non-spherical particle shape is represented by clustered spheres. To perform reliable DEM-CFD simulations, we obtain the DEM contact parameters by an experimentally driven calibration procedure. Our strategy to model optical sorting by DEM-CFD is motivated by the qualities of this approach: While computing times are relatively small, the results yielded can be analyzed in detail, and large particle systems can be handled. Although being used throughout many industries, there is very little research concerning the numerical investigation of optical belt sorters [16]–[19]. The uncoupled DEM is used broadly to address pure conveying problems, especially to analyze wear and load [20]–[22]. Coupled DEM-CFD simulations are prominent in other topics, such as pneumatic conveying [23], fluidized beds [24] and many others [25]–[27]. For a comprehensive overview of possible methods, limits as well as applications of the DEM-CFD, we refer the reader to [28].

Our article is structured as follows: The following Section 2 explains the methodology we used for the DEM-CFD simulations. Section 3 contains the description of our sorter model and the material representation in the DEM-CFD with calibration results. In Section 4, the consequences of changing the belt velocity for the bulk material and the affected components of the sorting are discussed. Section 5 presents the derivation of our optimization framework to operate the belt sorter at varying belt velocities and the derivation of related optimized parameters. In Section 6, the optimized parameters are applied to the DEM-CFD for a sorter operated at varying belt velocities for validation. Furthermore, real sorting scenarios with two different nozzle activation speeds are assessed, and corresponding results are shown. Finally,

Section 7 draws conclusions from the findings. The calibration procedure of the DEM contact parameters is described in Appendix A.

## 2 Methodology: DEM-CFD approach

To describe particle movements within the DEM, we start with the second Newtonian law of motion governing translational motion for particle  $i$  with the mass  $m_i$  and acceleration  $\ddot{\vec{x}}_i$

$$\ddot{\vec{x}}_i m_i = \overrightarrow{F}_i^c + \overrightarrow{F}_i^g + \overrightarrow{F}_i^f, \quad (1)$$

where  $\overrightarrow{F}_i^c$  are summed contact forces originating from contact with other particles and walls,  $\overrightarrow{F}_i^g$  is the gravitational force, and  $\overrightarrow{F}_i^f$  is the force caused by interaction with the surrounding fluid. Analogously, rotational motion is governed by

$$J_i \dot{\vec{\omega}}_i + \vec{\omega}_i \times (J_i \vec{\omega}_i) = \Lambda_i^{-1} (\overrightarrow{T}_i^c + \overrightarrow{T}_i^r), \quad (2)$$

where  $\overrightarrow{T}_i^c$  are the summed torques induced by wall and particle interactions through sliding friction and  $\overrightarrow{T}_i^r$  by rolling friction,  $J_i$  is the mass tensor of inertia, and  $\dot{\vec{\omega}}_i$  denotes the angular acceleration both in the body fixed frame. A vector e.g. a torque is transformed from the global frame to the body fixed frame by  $\Lambda_i^{-1}$ . Note that no torques are induced by fluid interaction as no submodels for particle-fluid torques are applied and the fluid force  $\overrightarrow{F}_i^f$  causes no torques.

Adopting the approach from [19] and as also common within the DEM, the occurring contact forces  $\overrightarrow{F}_i^c$  are split into a normal and a tangential part for contact modelling.

Normal contact forces  $\overrightarrow{F}^n$  are described by a linear spring damper model

$$\overrightarrow{F}^n = k^n \delta \vec{n} + \gamma^n \vec{v}_{rel}^n, \quad (3)$$

with normal spring stiffness  $k^n$ , virtual overlap  $\delta$ , normal vector  $\vec{n}$ , normal damping coefficient  $\gamma^n$  and the relative velocity at the contact point  $\vec{v}_{rel}^n$ . For the linear spring damper model, the spring stiffness and damping coefficient can directly be calculated from coefficients of normal restitution between particle–particle and particle–wall interactions and the predefined collision time [29].

The tangential force  $\overrightarrow{F}^t$  is calculated from a linear spring model and assumed to be limited by Coulomb friction

$$\overrightarrow{F}^t = \min \left( k^t \left| \overrightarrow{\xi}^t \right|, \mu_c \left| \overrightarrow{F}^n \right| \right) \vec{t}, \quad (4)$$

where  $k^t$  is the tangential spring stiffness,  $\left| \overrightarrow{\xi}^t \right|$  is the absolute value of tangential displacement and  $\mu_c$  is the coefficient of Coulomb friction. The tangential vector is denoted by  $\vec{t}$ .

To model rolling resistance  $\overrightarrow{T}_i^r$  in eq. (2), a model provided by [30] is adapted. The rolling torque can be calculated from the coefficient of rolling friction  $\mu_r$ , the normal force  $\overrightarrow{F}^n$ , the rolling radius  $R_r$  and the relative angular velocity  $\overrightarrow{\omega}_{rel}$ ,

$$\overrightarrow{T}_i^r = -\mu_r \left| \overrightarrow{F}^n \right| R_r \frac{\overrightarrow{\omega}_{rel}}{\left| \overrightarrow{\omega}_{rel} \right|}. \quad (5)$$

The fluid phase as part of the nozzle jet is modeled separately for our setup and is described by conservation of mass (eq. (6))

$$\frac{\partial \rho_f}{\partial t} + \nabla \left( \rho_f \overrightarrow{u}_f \right) = 0 \quad (6)$$

and conservation of momentum (eq. (7)), respectively

$$\frac{\partial (\rho_f \overrightarrow{u}_f)}{\partial t} + \nabla \left( \rho_f \overrightarrow{u}_f \overrightarrow{u}_f \right) = -\nabla p + \nabla \tau + \rho_f \overrightarrow{g}. \quad (7)$$

In Eqs. (6) and (7)  $\rho_f$  is the fluid density,  $\overrightarrow{u}_f$  the fluid velocity,  $p$  the pressure,  $\overrightarrow{g}$  the gravitational acceleration and  $\tau$  the stress tensor. For turbulence modeling, we use the Reynolds-averaged Navier-Stokes equations, so that the stress tensor can be written as

$$\tau = \eta_e \left[ (\nabla \overrightarrow{u}_f) + (\nabla \overrightarrow{u}_f)^{-1} \right], \quad (8)$$

where  $\eta_e$  is the effective viscosity which is obtained through turbulence modeling. In doing so, we introduce additional equations and can solve Eqs. (6) and (7). Details of the used turbulence model are given in Section 3.1.1.

DEM and CFD are coupled one way, which means that the solid phase is disturbed by the fluid, but not vice versa. Therefore, Eqs. (6) and (7) are not considering the local fluid fraction  $\varepsilon_f$ , and the particle-fluid interaction force is not applied volumetrically. As a consequence,

phenomena such as slipstream introduced by particles on other particles are not covered by our model.

The fluid force  $\vec{F}_i^f$  onto the particles is calculated by a drag-force correlation, which is the reason why our model is referred to as unresolved DEM-CFD. The exact flow profile around a particle is not computed but averaged and used to calculate an integral drag force, which acts at the particle centroid. We use the drag model introduced by [31], since it is applicable to complexly shaped particles. It is written as

$$\vec{F}_i^f = \vec{F}_i^D + \vec{F}_i^{\nabla p} = \frac{1}{2} \rho_f |\vec{u}_f - \vec{u}_p| c_D A_{\perp} \varepsilon_f^{1-\chi} (\vec{u}_f - \vec{u}_p). \quad (9)$$

The acting force is the sum of the drag  $\vec{F}_i^D$  and pressure gradient force  $\vec{F}_i^{\nabla p}$ . Velocities of fluid and particles are denoted by  $\vec{u}_f$  and  $\vec{u}_p$ , respectively.  $c_D$  denotes the drag coefficient of a particle,  $A_{\perp}$  the projection area perpendicular to the flow direction, and  $\varepsilon_f$  is the local fluid porosity. It holds that  $0 < \varepsilon_f < 1$  due to the solid phase in the fluid.  $\chi$  is an empirical correction factor and depends on the particle Reynolds number  $Re$  by

$$\chi = 3.7 - 0.65 \exp\left(-\frac{(1.5 - \log(Re))^2}{2}\right). \quad (10)$$

The Reynolds number for a particle is given by

$$Re = \frac{1}{\eta_f} \varepsilon_f \rho_f d_p |\vec{u}_f - \vec{u}_p|. \quad (11)$$

Particle diameter and fluid viscosity are denoted by the volume-equivalent quantity  $d_p$  and  $\eta_f$ , respectively. The drag coefficient is computed from a correlation that was derived by [32] for non-spherical particles and is written as

$$C_D = \frac{8}{Re} \frac{1}{\sqrt{\phi_{\perp}}} + \frac{16}{Re} \frac{1}{\sqrt{\phi}} + \frac{3}{\sqrt{Re}} \frac{1}{\phi^{3/4}} + 0.42 \cdot 10^{0.4(-\log(\phi))^{0.2}} \frac{1}{\phi_{\perp}}, \quad (12)$$

where  $\phi_{\perp}$  is the ratio of the cross-sectional area of a volume equivalent sphere to the cross-sectional area of the particle perpendicular to the flow. The ratio of the surface area of a volume equivalent sphere to the surface area of the particle is denoted by  $\phi$ . It is referred to as the sphericity.



### **3 Considered sorting setup**

#### **3.1 Numerical model of the optical belt sorter**

The dimensions and outline of the investigated sorting system are adapted from a laboratory-scale real sorting system, as shown in Fig. 2 (a). The feeding system was removed, and the components were simplified. An overview of the sorter setup can be seen in Fig. 2 (b). The sorter is fed by a continuous particle inlet (1), that controls the inflowing mass flow and the proportion of the material mixture. A chute (2) reduces vibrations of the material and pre-accelerates it. On the belt (3) the material is accelerated and transported to the detection stage (4), where image acquisition and successive data processing take place. The detection stage is either an area of 10 cm length (4a – 4b) for area-scan, camera-based sorting or a line (4b) for line-scan or ideal constant velocity sorting. If reject material that has to be sorted out is detected, nozzles are activated at the separation stage (5), and the particles are ejected into the reject container (6). The accept material can pass the separation stage without being deflected and is collected in the accept container (7).

The conveyor belt is 554 mm long and 140 mm wide. The accept and reject containers and nozzle positions, as well as their orientations, are adjustable in x- and z-direction. The exact position is bulk material dependent, since its friction parameters and flow resistance vary. Besides the latter parameters, further crucial parameters for the sorting process are the activation duration of the nozzles  $\Delta t$ , the sorting model (see Section 3.1.2) and the nozzle time lag, which will be explained in Section 3.1.3. Note that all mentioned parameters are commonly fixed for a particular sorting operation.

The numerical model of the experimental system was extensively compared against experiments in [33]. Here, we have studied the transport behavior of the bulk material on the conveyor belt. Additionally, the sorting accuracy of the numerical and the experimental system was compared for three input compositions at two different mass flows at a fixed conveyor belt velocity, totaling 6 scenarios. By that, not only the particle model (DEM), but also the particle-fluid interaction (DEM-CFD) was validated. The numerical model was found to reproduce the transport behavior with more than 95 % accordance in the majority of cases. The sorting results

of the simulations matched the experiments with more than 95 % in all investigated cases. For further details see [33].

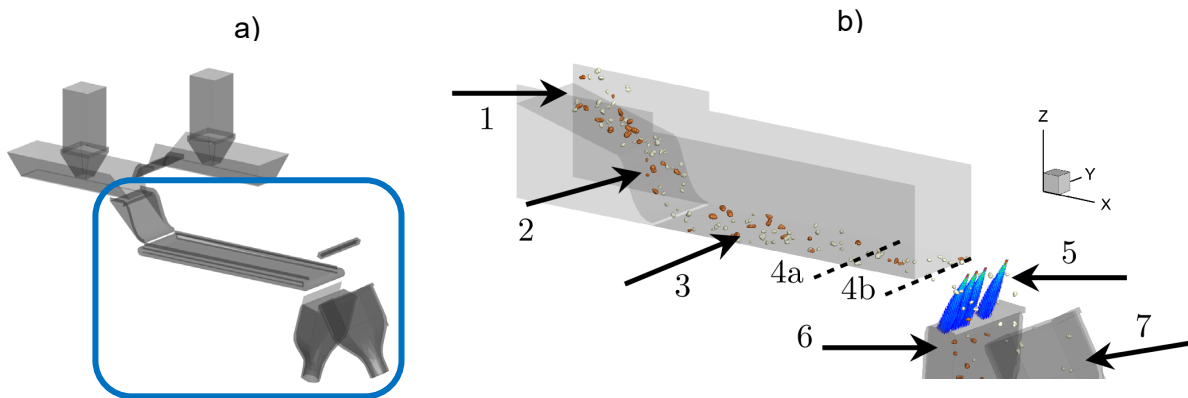


Fig. 2: Model of the laboratory scale optical sorting system (a). The blue frame indicates the part of the system that is simplified and used for the investigations in this work (b).

### 3.1.1 Model of the fluid jets

Fig. 3 (a) shows the geometry of a typical single nozzle as it is used for optical sorters. The geometry was imported from the real sorting system, which was mentioned before. It consists of one inlet and two outlets with a diameter of  $1.6 \text{ mm}$  each. The computation of the resulting fluid field as required for the DEM-CFD was done with Ansys Fluent 19.2. We used a stationary incompressible RANS with a realizable  $k-\epsilon$  turbulence model that is well suited for free stream flows. Thus, eqs. (6) and (7) apply. Common model constants were used for the simulation [34]: A turbulence intensity of 3 % and a turbulent viscosity ratio of 8 were assumed. The inlet pressure was  $1.5 \text{ bar}$ . The converged simulation result is shown in Fig. 3 (b) as a contour plot of the absolute velocity magnitude. One can observe the characteristic features of a free stream jet, which consist of the decay of the core stream velocity and the crosswise spread of the velocity profile [35]. Furthermore, we can locate the so-called merging point (MP) (see Fig. 3 (b)), which is found where the inner shear layers of the jets originating from the two outlets (see Fig. 3 (a)) converge. Another characteristic point, the combined point (CP), is located further downstream and designates the region where the profile of the dual free stream jet

corresponds to that of a single free stream [36]. Fig. 3 (c) shows a plane cut through the jet at a 3 cm distance from the outlet. This distance becomes important in Section 5.1.1.

To prepare the fluid field for coupling with DEM simulations, it was coarsened from about 5 million cells to roughly 10,000 cells. The fine CFD resolution is not needed for unresolved DEM-CFD coupling and would slow down computations unnecessarily. The whole nozzle array with 32 nozzles was obtained by concatenating the coarsened single nozzle field 32 times. 16 of 32 activated nozzle fields are shown in Fig. 3 (d).

In the sorting process, 1-3 nozzles are activated to target a detected particle, depending on the particle size in the y-direction. A single nozzle covers a width of 5 mm in the real sorting system [37], so that the length of the whole bar is 16 cm in y-direction. Note that the air resistance during free flight of particles is neglected.

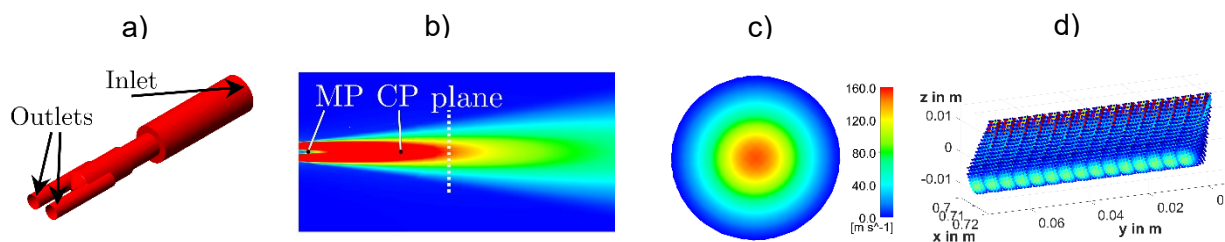


Fig. 3: Geometry of a single nozzle (a), its related fluid field as a contour plot (b), a plane cut at 3 cm from the outlet (c) and half of the resulting fluid field of the whole nozzle bar (d).

### 3.1.2 Applied sorting models

In the following, the three sorting models that were used for the present study are presented briefly. The purpose of the models is the prediction of a particle trajectory between the detection stage (camera) and the the separation stage (nozzle array). On that basis, the nozzles are triggered, and the activation time is computed. Note that the activation time is not necessarily identical to the formation of the fluid jet and depends on the time lag of the nozzle, which will be explained in the next Section 3.1.3. The exact location to which the sorting model must predict the particle movement to assure optimal separation is significant. This location will be optimized in Section 5.1.1. It is clear that the prediction quality of the used sorting model

is crucial for the overall sorting accuracy. A necessary requirement for the working principle of an optical sorter is therefore the optical distinction of particles by the sorting model. This excludes stacking material on the conveyor belt, where the lower layer of material is not visible and thus cannot be targeted properly, strongly reducing the accuracy of the whole sorting system. Such scenarios mark the operational limit of optical belt sorting and are consequently excluded from the investigations in this study.

**Line-scan, camera-based sorting:** The particles are detected by a line-scan camera at the last x-position in the transport direction of the conveyor belt as close as possible to the nozzle array (see Fig. 4 (a)). A passing particle's y-position can be identified in the camera image, the y-velocity component orthogonal to the transport direction is typically assumed to be zero. The velocity in the x-direction is typically assumed to be constant with a predefined value because it is not captured by the camera. In our sorter model, the assumed velocity is chosen to be equal to the average particle velocity at the detection stage  $\bar{v}$  obtained by preliminary DEM-CFD simulations, because slippage between particles and conveyor belt may occur, and therefore the conveyor belt velocity is not a suitable choice for  $\bar{v}$ . Line-scan camera based sorting is the standard sorting method applied in industry-scale sorters [38].

**Area-scan, camera-based sorting:** In this prediction procedure, the particles are tracked over a certain belt length, see Fig. 4 (b). Thus, this method is also referred to as tracking. Multitarget tracking, combined with Kalman filter estimation, is utilized for positional and velocity prediction of the tracked particles [39]. During the tracking phase, the state of each particle is subsequently estimated based on the measurements and used to predict the next state. The final prediction for the particular nozzle at which the particle arrives and the time of the nozzle activation is done between the last particle measurement and nozzle array. Calculations are performed under the assumption that the velocity remains constant. For further details concerning the algorithm and performance comparisons, see [19], [40]–[43]. The tracking is realized as a MATLAB routine, which runs parallel to the DEM-CFD simulation and exchanges

data with the simulation code, as shown in Fig. 4 (c). This method showed to yield improved sorting results compared to the standard line-scan, camera-based sorting, which, among other reasons, is due to a prediction of the y-velocity component of the particles.

**Ideal constant velocity:** This prediction method is a numerical benchmark model applicable as part of the DEM-CFD. It makes use of the exact, numerically known velocity in x- and y-direction  $v$  at the detection stage. Nozzle ID and activation time are then calculated under the assumption of a constant velocity between the detection stage (camera) and separation stage (nozzle array), as shown in Fig. 4 (d). This model will be referred to as ideal constant velocity (ICV) in this work.

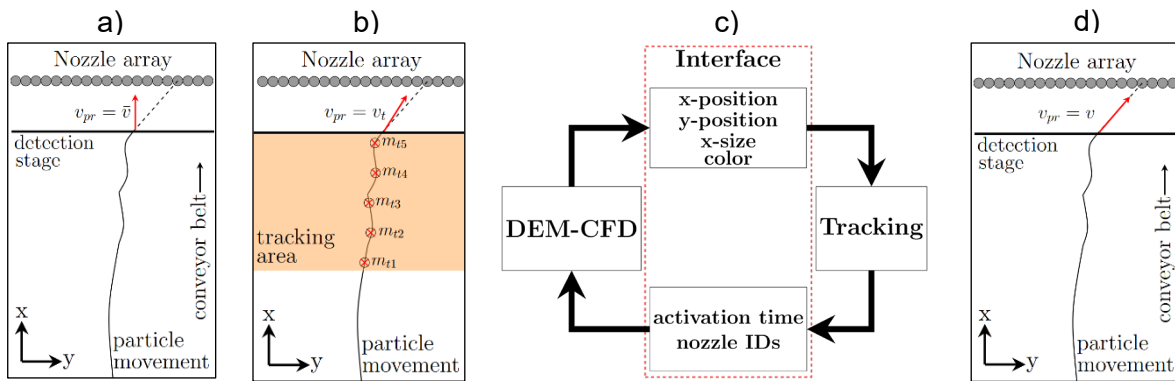


Fig. 4: Employed prediction models for sorting: a) line-scan camera, b) area-scan, camera-based sorting, c) its realization in the DEM-CFD, and d) ideal constant velocity (ICV) prediction.

### 3.1.3 Nozzle operation modes

Two operation modes of nozzle activation were considered in our DEM-CFD model, namely instantaneous and lagged. This is because, in reality, nozzles need a short timespan to be triggered and to mechanically open and close and therefore cannot be used arbitrarily fast one after another. The lag is caused by data processing time, electrical signal transmission time and nozzle valve opening or closing, respectively. Nozzles are, therefore, automatically operating lagged in real sorting systems. In other words, a nozzle is not activated at the desired time, but a short period later. The lag time depends on the type of nozzle used (see [44]). Since

the numerical model is not limited by mechanical or electrical delays, it is possible to study the influence of the lag time on the sorting accuracy, which is done in Section 6.2. In the sorter described in [37], lag times of around 5 ms were found, which we will also use for our investigations. The principle of both activation modes is illustrated in Fig. 5. It shows possible scenarios in a series of nozzle activations for an exemplary activation duration of 10 ms. In scenario (a), we see that instantaneous nozzles can be activated arbitrarily fast due to absence of any lag at which it is opened or closed. The activation time is marked by the red line at the beginning of an activation period. When a nozzle is operated in lagged mode, the influence of the lag depends on the time between the points of activation. A nozzle can be activated at the desired point of time if there is sufficient time to account for the opening lag (b). As the activation times move closer together, a shortening of activation duration can occur due to the preceding nozzle opening (c). In the worst-case scenario (d), a whole activation period is blocked by preceding nozzle activation. As particle velocities increase at higher conveyor belt velocities, the time lag of nozzle activation will be important for sorting accuracy, which will be shown in Section 6.2.

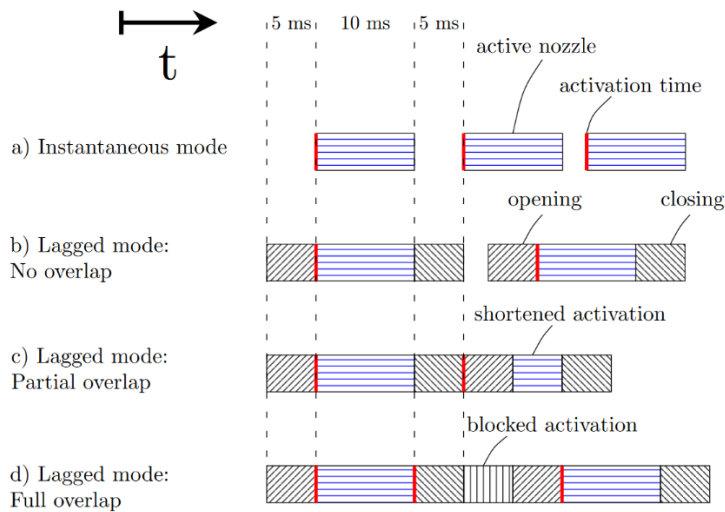


Fig. 5: Illustration of the two operation modes: Instantaneous and lagged. Outlined in four different scenarios with an exemplary activation duration of 10 *ms*. Active nozzles are indicated by blue horizontal lines, and opening and closing durations are shown as skew lines. Activation time is indicated by a red line. Instantaneous nozzles can be activated arbitrarily fast (a). In lagged mode, a nozzle needs an additional 5 *ms* to open and close, respectively. This may be without influence (b), but can also lead to shortening (c) or blocking (d) of the activation period, depending on the temporal spacing between the activation times.

## 3.2 Material model

### 3.2.1 Considered materials

For a realistic sorting scenario, brick (Fig. 6 (a)) and sand-lime brick (Fig. 6 (c)) have been chosen. By sieving analysis, a particle size distribution was obtained based on the smallest particle dimension, see Fig. 6 (b) and (d). Sizes of 3.5 *mm* to 5.65 *mm* were chosen for representation of both materials, since they account for more than 80 % of the material bulk. Density analysis yielded 2541 *kg/m*<sup>3</sup> for brick and 2565 *kg/m*<sup>3</sup> for sand-lime brick.

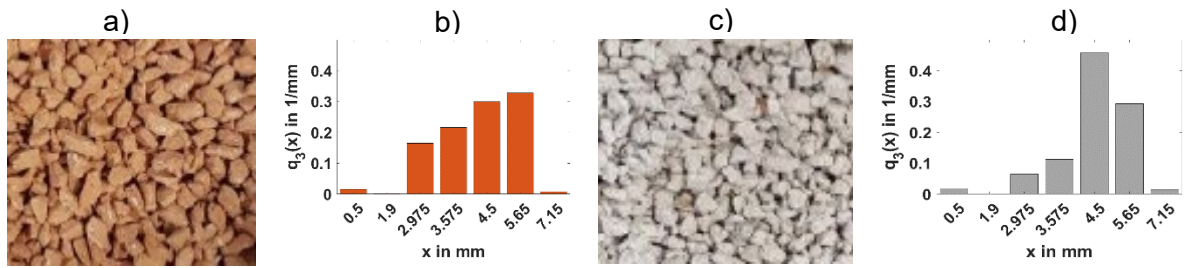


Fig. 6: Brick material (a) and its size distribution (b) and sand-lime brick (c) and its size distribution (d).

### 3.2.2 Particle representation for simulations

Based on size analysis, a CT scan of a representative selection of particles was conducted. A clustering approach was employed since there exist faster and more robust contact detection algorithms for clustered shapes that cut computing time drastically. Up to 20 spheres were used to approximate the complex hulls by utilizing an optimization algorithm that minimizes the protruding sphere volume. Fig. 7 shows the CT scanned particles (a, c) and the resulting clusters (b, d) for two examples. In order to model the variation of particle shapes, 3 – 5 shapes were identified for each size class. As a result, brick is represented by 11 particle types, sand-lime brick by 13 types. Moments of inertia of the particles were calculated according to [45]. The particle shape was approximated by a large number of points, with a virtual volume being assigned to each point. The moments of inertia were determined by the volume in the corresponding coordinate direction. The error introduced by the utilized drag correlation in eq. (12) is around 14.5 % in average, depending on the exact particle shape. Considering the shapes of the approximated particles, the error caused by the drag correlation can be assumed to be around 12 %, because cylindrical or cuboid shapes are not used [32]. The authors additionally state that the error is likely to be less, because the experimental data used to calculate the error shows broad scattering. The use of a resolved DEM-CFD approach, where the fluid around the particles is solved in detail directly yielding the drag, would increase the computational cost and complexity of the simulations by several orders of magnitude, as a much finer time step would be required as for unresolved DEM-CFD simulations. In addition,



the coupling region in the area of the nozzle jets would have to be remeshed around each particle as they move through the fluid field. In highly loaded particle systems as investigated in Sec. 6, there may be present more than 20 particles at once in the coupling region. For a broad parameter study with a large number of simulations, such an approach (resolved DEM-CFD) would not be realizable.

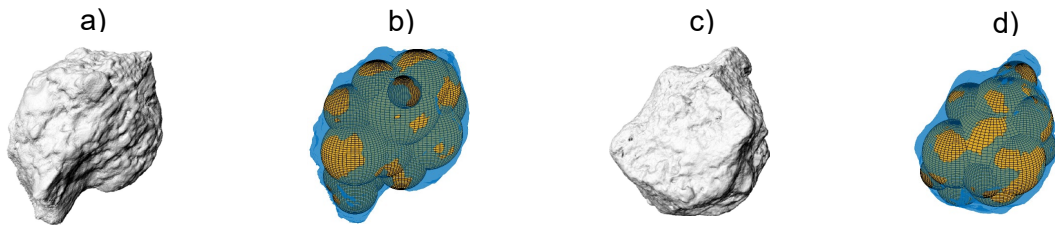


Fig. 7: Triangular mesh from particle CT-Scan (a, c) and the same particle represented by a cluster of spheres (b, d) shown for two different particles.

### 3.3 DEM contact parameters

As a next step, calibration of DEM contact parameters was carried out. The general procedure of calibration is to conduct small-scale experiments and simulate them, while parameters of interest are varied until the results of simulations and experiments match, partly adapting the procedure of [46]. For a detailed outline of the calibration procedure, see Appendix A. The parameters obtained by calibration are summarized in Tab. 1. Note that parameters for the contact of both materials with each other were determined by averaging the values of the single material contacts for simplification. This is valid since both materials behaved similarly in all calibration experiments and contact parameters differ only marginally. Note further that all obtained contact parameters can be either directly applied in the DEM or, in the case of the COR, be used to calculate a normal stiffness  $k^n$  and a damping coefficient  $\gamma^n$  (both required for Eq. (3)) based on a predefined time for a collision, which was set as  $t = 5 \cdot 10^{-4} s$ . Each collision was resolved by 50 steps, resulting in a simulation time step of  $t = 1 \cdot 10^{-5} s$ . The tangential stiffness  $k^t$  (see Eq. (4)) is calculated as stated in [47] based on mechanical material properties.

Material	Sand-lime brick	Brick
COR P-SB [-]	0.19	0.215
COR P-B [-]	0.215	0.24
COR P-CB [-]	0.19	0.1
COR P-SW [-]	0.19	0.1
Sliding friction P-SB [-]	0.19	0.18
Sliding friction P-B [-]	0.18	0.17
Sliding friction P-CB [-]	0.4	0.56
Sliding friction P-SW [-]	0.4	0.56
Rolling friction P-SB [-]	$2 \cdot 10^{-2}$	$1.2 \cdot 10^{-2}$
Rolling friction P-B [-]	$1.2 \cdot 10^{-2}$	$3.8 \cdot 10^{-3}$
Rolling friction P-CB [-]	$7.5 \cdot 10^{-3}$	$5.8 \cdot 10^{-3}$
Rolling friction P-SW [-]	$7.5 \cdot 10^{-3}$	$5.8 \cdot 10^{-3}$

Tab. 1: Final calibrated parameters for simulations. (P) refers to the contacting particle, either sand-lime brick or brick that comes into contact with either sand-lime brick (SB), brick (B), conveyor belt (CB) or sorter wall (SW) material.

#### 4 Sorter operation at adaptable conveyor belt velocities

With the numerical model of the optical belt sorter, a systematic study of the sorter at various conveyor belt velocities was conducted. Firstly, the bulk behavior on the conveyor belt was investigated. No subsequent sorting was performed in the simulations. Secondly, those components of the sorting system were identified, which were subject to the adjustment to changed belt velocities. The identification was made with regard to the particle trajectory in the free flight phase, which is highly impacted by the belt velocity.

##### 4.1 Characteristics of bulk transport

To gain insight into the bulk behavior on the conveyor belt, numerical simulations were run at two mass flows with a pure material stream of the respective materials. Simulations were run

at mass flows of 100  $g/s$  and 500  $g/s$ , and conveyor belt velocities of 0.9  $m/s$  to 2.9  $m/s$  varied in 0.2 steps. The simulations were chosen such that they coincide with the sorting simulations in Section 6. Fig. 8 shows the average particle velocity at the conveyor belt end in (a) and the occupancy density on the conveyor belt in (b). The occupancy density is defined by the fraction of the total belt area that is particle-covered.

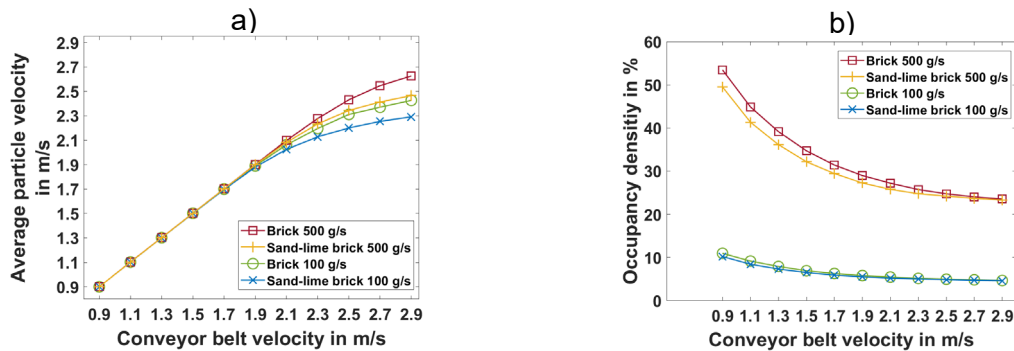


Fig. 8: (a) Mean particle velocity when entering the free flight period versus the belt velocity for brick and sand-lime brick at 100  $g/s$  and 500  $g/s$ . (b) Occupancy density as a function of the belt velocity for brick and sand-lime brick at 100  $g/s$  and 500  $g/s$ . Both shown evaluated at conveyor belt velocities of 0.9  $m/s$  to 2.9  $m/s$  varied in 0.2 steps.

The average particle velocity along the belt increases proportionally with belt velocity up to 1.9  $m/s$ , as shown in Fig. 8 (a). At higher belt velocities, particle slip occurs, and the curve flattens depending on material and mass flow. This is a general phenomenon of material conveying and depends on the specific conditions, such as transported material and belt friction [48]. Sand-lime brick is accelerated less than brick due to smaller friction on the conveyor belt (comp. Tab. 4). At 100  $g/s$ , sand-lime brick reaches a maximum velocity of 2.28  $m/s$  in average while brick reaches a velocity of 2.42  $m/s$  at 100  $g/s$ . Furthermore above 1.9  $m/s$  the distribution of the particle velocity along the belt broadens (not shown here). In Fig. 8 (b), there is a clear trend of decreasing occupancy density for belt velocities up to 2.3  $m/s$ . Particles are pulled apart faster from each other at increasing belt velocities, leading to improved singulation. This effect is much more prominent for sorting scenarios at 500  $g/s$  ,

where occupancy density decreases from around 50 % to roughly 30 % from 0.9 – 2.1 *m/s*. At higher belt velocities it is diminished by dominating particle slip.

These findings have some important implications for the design and operation of optical belt sorters and the configuration of the separation stage. Obviously, there exist conveyor belt velocities where slip is increasingly present. At those velocities, economic operation is not feasible. Such velocities should therefore be avoided. For sorting setups operated below these velocities, however, decreased occupancy density present at elevated belt velocities can be useful in order to reduce undesirable clustering of particles, leading to less densely distributed scenarios on the belt. When the sorting setup is arranged for a certain belt velocity, it must be assured that the bulk is moving with the velocity of the belt. Otherwise, the actual bulk velocity has to be accounted for.

#### **4.2 Velocity-dependent sorter components**

To adapt the sorting stage of the belt sorter to changing conveyor belt velocities, the positions and alignments of the components have to be chosen such that both fractions fall in the respective containers. Due to changed particle trajectories, the accept container must be moved along the x-axis. This was the only direction in which the accept container was allowed to be moved. For the reject material, more factors must be taken into account: Since it is deflected into the reject container by the fluid jet, the positions of the nozzle and reject container are interrelated. Thus, a movement of the nozzle affects the reject container and vice versa. To assure an optimal entry angle of the reject particles into the container, the alignment of both the nozzle and the container must also be re-adjusted. Fig. 9 shows the sorting stage of the sorter model in the initial positions and alignments (a) and with the adjustable components in a different position and alignment (b).

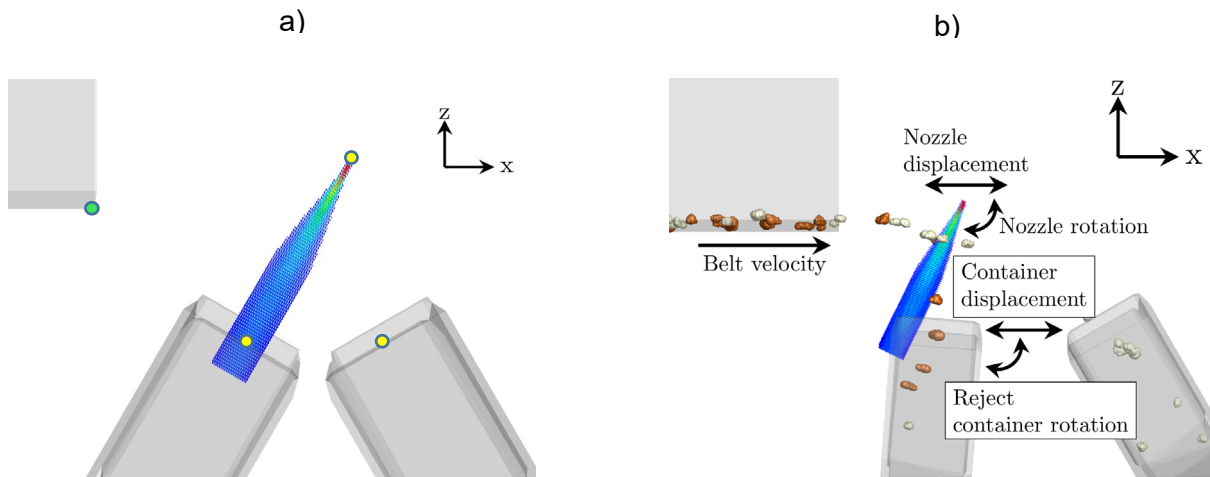


Fig. 9: Close view of the sorting stage with activated nozzles. (a) Components in the initial configuration. The yellow dots represent the center points of the components, along which they were moved and rotated. Positions are measured from the edge of the belt, marked by the green dot. (b) The colored fluid jet deflects orange brick particles into the reject container in a changed configuration. White sand-lime brick particles are collected in the accept container. Arrows denote degrees of freedom of the sorter components.

To bound the complexity of the problem, z-positions were kept fixed for all components. Furthermore, to have mobile components adjustable in only one coordinate direction simplifies the implementation of adaptive components into a real sorting system. The components are summarized with their initial position, alignment and degree of freedom in Tab. 2.

Component	Initial position	Degree of freedom
Nozzle angle	60.4 °	Rotation around y-axis
Nozzle position	$x = 8.0 \text{ cm}$ $z = 0.8 \text{ cm}$	x-axis
Reject container angle	29.6 °	Rotation around y-axis
Reject container position	$x = 3.32 \text{ cm}$ $z = -7.74 \text{ cm}$	x-axis

Accept container	$x = 13.27 \text{ cm}$	x-axis
position	$z = -7.74 \text{ cm}$	

Tab. 2: Adjustable components of the sorter with their initial positions and alignments. Positions are given from the point of origin at the edge of the conveyor belt, denoted in green in Fig. 9 (a). Alignments are measured as depicted in Fig. 10 (a).

While the positioning of the accept container is straightforward, the adjustment of the nozzle and reject container are governed by the particle-fluid interaction taking place during the flight through an activated nozzle. Due to the coupling of the equations and the diversity of the particles being ejected, a direct solution is not possible. Instead, problem reduction and optimization are applied to obtain optimal configurations of the sorting stage for arbitrary conveyor belt velocities.

## 5 Adjustment of the sorting setup to arbitrary conveyor belt velocities

### 5.1 Adjustment procedure

In this Section 5.1, we present a framework that allows us to find optimal sorter parameters for arbitrary particle velocities. It was implemented in MATLAB. The aim of the MATLAB framework was to reduce the computation time of particle fluid interactions – taking place at the separation stage – drastically compared to the 3D DEM-CFD, while retaining its accuracy. By doing so, several thousand computations were run within minutes using an optimization algorithm that searched the parameter space for the optimal setup. The results in terms of operational parameters were then used for DEM-CFD simulations, which will be presented in Section 6.

All assumptions that have been made to derive the simplified sorter model for optimization are explained in the next Section 5.1.1. Afterwards, the general optimization procedure and the construction of the objective function will be described. Section 5.2 presents the configuration parameters yielded by making use of the framework.

### 5.1.1 Simplified sorter model used for optimization

In order to make the best use of optimization methods, a fast computation of the objective function is needed. For our problem, the objective function is directly related to the particle flight through the fluid jet originating from the nozzle array. Since we want to rearrange and optimize the sorting setup depending on the belt velocity and the thereby resulting particle velocity, the trajectories must be computed readily.

A large reduction of computing time can be achieved by reducing our problem from three to two dimensions in physical space. In the following, we present the assumptions we made for that simplification.

- 1) The particles are calmed on the conveyor belt. They move with belt speed and do not move orthogonally to the transport direction.
- 2) At a certain distance from the nozzle array, the fluid field is nearly homogenous, meaning that the third dimension (here:  $y$ ) can be neglected. Obviously, this area must be downstream of the combined point (CP) of the twin jet field (see Fig. 3 (b)), where both jets unify. For our nozzle array configuration, this distance was chosen at 3 cm from the nozzle outlet see Fig. 3 (c) and (d).
- 3) To calculate the drag onto the particles, we can use the drag formula for single particles as an approximation neglecting particle orientation. The drag force is given by  $F_D = c_D \cdot \frac{\rho}{2} \cdot A \cdot v_{rel}^2$ , with  $c_D$  being the drag coefficient,  $A$  the particles projection area perpendicular to the fluid velocity,  $\rho$  the fluid density and  $v_{rel}$  being the relative velocity between particle and fluid.
- 4) The bulk material can be represented by a few representative particle shapes and sizes.

The projection areas and masses of each material were analyzed, and the six most significant masses with maximum and minimum projection area for each were chosen. Hence, all combinations of mass and projection area were covered. The use of extreme combinations of

mass and projection area assures that all particles hit the containers. The value ranges are given in Tab. 3.

Quantity	Sand-lime brick	Brick
Projection areas	$1.7 \cdot 10^{-5} - 5 \cdot 10^{-5} \text{ m}^2$	$1.45 \cdot 10^{-5} - 8.6 \cdot 10^{-5} \text{ m}^2$
Masses	$1.45 \cdot 10^{-5} - 5.4 \cdot 10^{-4} \text{ kg}$	$1.2 \cdot 10^{-5} - 8 \cdot 10^{-4} \text{ kg}$

Tab. 3: Value range of projection areas and masses for both materials.

The projection areas and masses vary in the order of five, while the drag coefficient following eq. (12) varies at most by 20% for all particles around a value of 1. Thus, it is held constant at  $c_D = 1$  for optimization calculation. Force equilibrium and Newton's law of motion yield

$$\dot{v}_x \cdot m = A \cdot \rho \cdot \frac{1}{2} c_D \cdot \bar{v}_{rel} \cdot v_{x,rel}, \quad (13)$$

$$\dot{v}_z \cdot m = A \cdot \rho \cdot \frac{1}{2} c_D \cdot \bar{v}_{rel} \cdot v_{z,rel} - mg \quad (14)$$

for both coordinate directions denoted by the subscripts. The particle acceleration is referred to as  $\dot{v}$ , with the dot indicating the temporal derivative of  $v$ , the particle mass is  $m$ , and the gravitational acceleration is  $g$ . The equations are coupled by the absolute value of the relative velocity  $\bar{v}_{rel}$ .

A Forward-Euler scheme with a step of  $1 \cdot 10^{-4} \text{ s}$  was used for time integration. For each conveyor belt velocity and corresponding particle velocity and material, 12 particle trajectories were calculated.

### 5.1.2 Optimization strategy

In addition to the already presented geometrical parameters of nozzle bar and reject container, two temporal parameters were introduced, which were subject to the optimization: The first parameter is the duration of the nozzle activation  $\Delta t$ . The second parameter  $\tau$  denotes the activation time offset between a particle reaching the area of the fluid field and the point in time at which the nozzle is activated. This variable is crucial because it allows the algorithm to



activate the nozzle when the particle is near the core of the jet. Here, the fluid jet transfers the highest momentum to the particle and deflects it in the shortest time. In other words, through  $\tau$ , we obtained the optimal position  $x_A$ , at which the nozzle had to be activated, by  $x_A = v_p \cdot \tau + x_E$ , with  $v_p$  being the particle velocity and  $x_E$  being the edge of the fluid field. The position of nozzle activation  $x_A$  was then used in the specific sorting model to predict the time at which a particle reached the nozzle at  $x_A$  and thus the nozzle had to be activated. The geometric parameters were optimized as the deviation  $\Delta$  from the initial values as given in Tab. 2. Consequently, absolute positions and orientations are given by the initial value altered by the optimized  $\Delta$  for the respective variable. All parameters are summarized in Tab. 4. Note that a rotation ( $\Delta\alpha$ ,  $\Delta\beta$ ) is measured counterclockwise.

<b>Parameter</b>	<b>Variable name in optimization</b>
Nozzle rotation	$\Delta\alpha$
Nozzle displacement	$\Delta x_n$
Reject container rotation	$\Delta\beta$
Reject container displacement	$\Delta x_c$
Activation duration	$\Delta t$
Activation offset	$\tau$

Tab. 4: Optimized parameters with the symbol used in the optimization.

Fig. 10 (a) shows the input parameters, also referred to as optimization variables, in the simplified 2D simulation. Nozzle angle and container angle are shown in their initial position. Note that the particle trajectory is undisturbed during the time offset  $\tau$ . At its end, the nozzle activation starts for  $\Delta t$ . From there, a split up of the trajectories due to different masses and projection areas can be noticed.

The conditions and the respective optimal value for the construction of the objective function were defined as follows:

- I. Optimal distance between particle and nozzle outlet is 3 cm, when the nozzle is activated
- II. Intersection of deflected particle trajectory and reject container is at the container opening center at  $l_c/2 = 2.93 \text{ cm}$
- III. The angle between the deflected trajectory and the reject container opening is  $90^\circ$
- IV. The activation duration of the nozzle is minimal

Condition I was chosen so that particles pass through the jet region where high velocities and small gradients are prominent, as stated in Section 5.1.1 before. Conditions II and III assured that particles with non-optimal entry angles or positions still end up in the reject container. Condition IV minimizes undesired deflection of accept particles and furthermore saves compressed air, if applied to a real sorting system. Additionally, it was assured that the reject container did not intersect with the undeflected trajectories and the accept container. Otherwise, the algorithm would move the reject container back as far as possible to the trivial solution of an undeflected trajectory. Expressed in a function, the conditions yield

$$f(\Delta\alpha, \Delta\beta, \Delta x_c, \Delta x_n, \Delta t, \tau) = \sum_{i=1}^n (w_1(|l_i - 3 \text{ cm}|) + w_2(|l_i - \frac{l_c}{2}|) + w_3(|\theta_i - 90^\circ|) + w_4 IV_i). \quad (15)$$

The conditions were summed over  $n = 12$  trajectories per material so that they were evaluated for each particle. Weights  $w_1 - w_4$  scaled and weighted the conditions equally. The activation duration  $\Delta t$  and ejection delay  $\tau$  were optional input variables of the objective function, which could also be minimized on fixed positions and orientations of eject container and nozzle: Either  $w_1 - w_3$  or  $w_4$  could be set to zero.

The genetic algorithm from MATLAB was used to find the optima [49]. At least 30 generations with populations of 300 individuals were used. The stopping criterion was set at a function tolerance of  $1 \cdot 10^{-6}$ . Sorting setups were optimized for conveyor belt velocities of 0.9 m/s to 2.9 m/s in 0.2 m/s steps. Geometric parameter variation was simplified by using results of

preceding velocity optimization as an initial population for the next optimization. An exemplary result is shown in Fig. 10 (b), plotted for a single trajectory of brick for 1.1 – 2.7 m/s in 0.4 m/s steps. Also, conditions I-IV are depicted in the graphic.

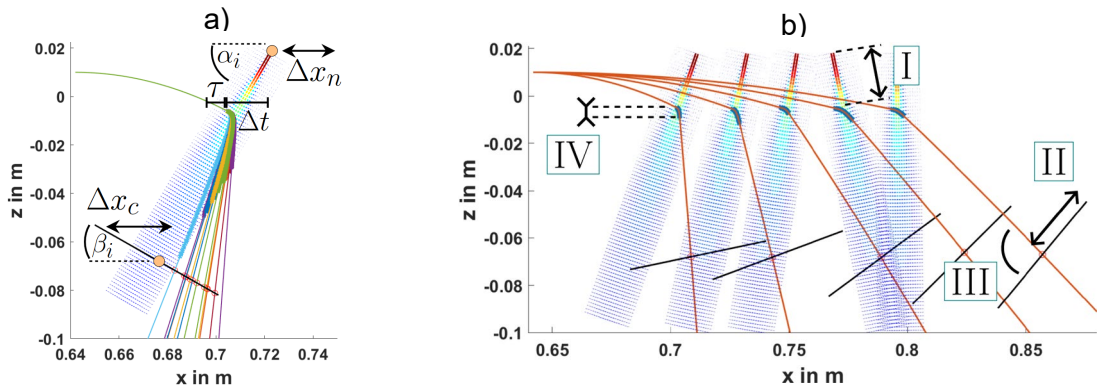


Fig. 10 (a): 12 trajectories of sand-lime brick through the activated nozzle with geometric and temporal input variables. The shown alignments are the initial ones of the container and nozzle ( $\alpha_i = 60.4^\circ$  and  $\beta_i = 29.6^\circ$ ). Orange circles locate the origin of the reject container and the nozzle at the initial position. (b): Exemplary results of optimizations, shown for particle trajectories of brick for conveyor belt velocities 1.1 – 2.7 m/s in 0.4 m/s steps. Also, optimization conditions (I-IV) are shown. Thick blue regions of the trajectories indicate the positions at which the nozzle jet was acting.

The optimization procedure was as follows:

O.1) Optimization of 4 geometric parameters ( $\Delta\alpha, \Delta\beta, \Delta x_c, \Delta x_n$ ) for a setup with a continuously operating nozzle (setting  $\Delta t = \infty$  s,  $\tau = 0$  s,  $w_4 = 0$ ).

O.2) Optimization of 2 temporal parameters ( $\Delta t, \tau$ ) on fixed positions and orientations ( $\Delta\alpha, \Delta\beta, \Delta x_c, \Delta x_n$ ) obtained as part of O.1 (setting  $w_1, w_2, w_3 = 0$ ).

The results of the optimizations are discussed in the next Section 5.2.

## 5.2 Adjustment results

The results of O.1 are shown in Fig. 11. From left to right, the plots show displacements and rotations from the initial positions and alignments of both reject container and nozzle, respectively. On the x-axis, the average particle velocity at the conveyor belt end that was used for optimization is shown. The respective optimization variable is plotted on the y-axis. The parameters for brick are plotted in blue, and parameters for sand-lime brick are plotted in red. Obviously, the range of particle velocities is narrower ( $0.9 \text{ m/s} - 2.7 \text{ m/s}$ ) than the actually used conveyor belt velocities of  $0.9 - 2.9 \text{ m/s}$  due to slip of the particles on the belt. This behavior was discussed in Section 4.1. The curves were interpolated piecewise between optimized parameters.

The optimized reject container rotation, see Fig. 11 (a), and displacement, see Fig. 11 (b), show a nearly linear progression with increasing particle velocity. This can be explained by increasing particle inertia: the particle trajectories are prolonged in the x-direction, so the container must adapt accordingly. Nozzle rotation, see Fig. 11 (c), and displacement, see Fig. 11 (d), also show a nearly constant ascent, while the curves are slightly offset for both materials. Several optimization runs showed that such changes in displacement directions, as well as oscillations in parameter curves, stem from the stochastic nature of the genetic algorithm. Since initial populations and following generations are chosen partly randomly, optimal solutions can vary between optimization runs with identical preferences [49]. In any case, the solutions fulfill our conditions in terms of optimality.

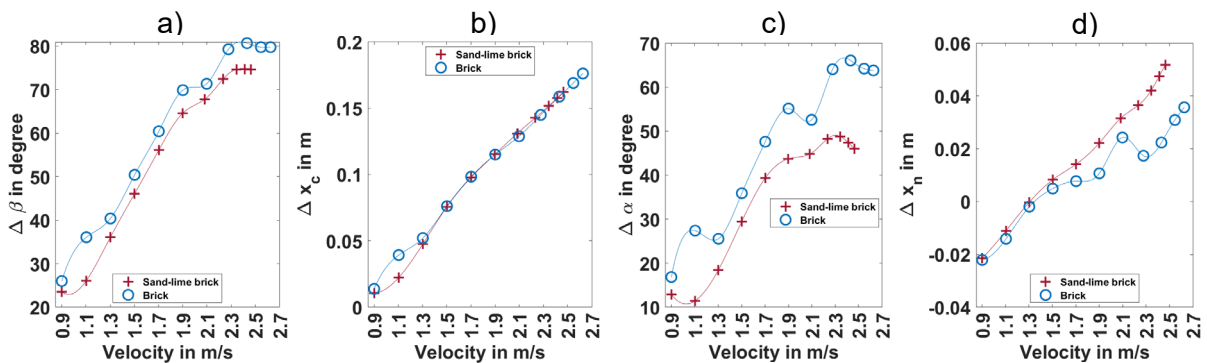


Fig. 11: (a) – (d) Displacements and rotations of reject container and nozzle array optimized for brick and sand-lime brick for a permanently operating nozzle ( $\Delta t = \infty$  s,  $\tau = 0$  s) in dependence on average particle velocity.

In Fig. 12, the optimization results of O.2 are presented. As already introduced, the temporal parameters were computed for an already fixed geometric arrangement of the nozzle and reject container at increasing conveyor belt velocities. Since the particle velocities were not equal for both materials, as can be seen in Fig. 8 (a), the velocities diverge towards higher values. In Fig. 12 (a), the activation duration  $\Delta t$  is shown. Both curves show oscillations, but obtained values also decline with increasing particle velocity. The decline is caused by a shrinking angle of deflection (angle between particle trajectory before and after nozzle interaction) at higher particle velocities, as obtained by O.1 (see also Fig. 10 (b)).

The activation offset (Fig. 12 (b)) decreases linearly with particle velocity for both materials. This happens as, due to higher velocity, the particles need less time to cover the distance between the fluid field edge and core.

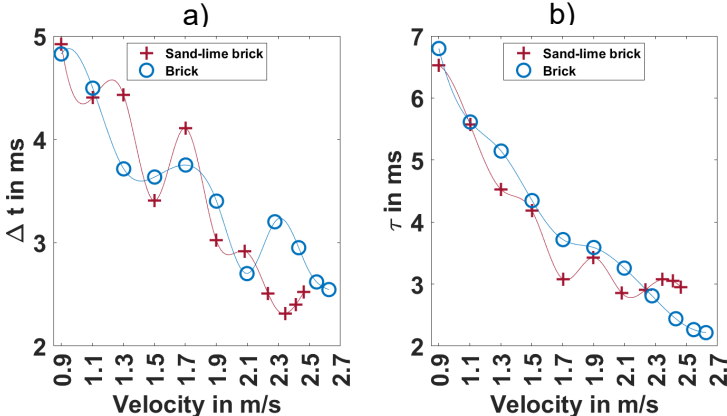


Fig. 12: (a) Optimized activation duration  $\Delta t$  of nozzles. (b) Optimized activation offset  $\tau$  in dependence on average particle velocity.

To sum up, the results show a clear tendency of moving the nozzle and containers further in the x-direction while increasing the nozzle and reject container rotation with increasing belt velocity. Due to this rearrangement, nozzle activation duration can be further reduced for faster particles.

## 6 DEM-CFD simulation results of the optimized sorter setups

The adjustment results corresponding to an average particle velocity aligned to that from Section 4.1 were applied to our DEM-CFD model of an optical belt sorter utilizing unresolved one-way coupling. First, it was verified that the obtained parameters were valid for a single component material stream. This was proven for both geometrical (O.1) as well as temporal parameter sets (O.2), outlined in Section 6.1. After evaluating the optimal sorting parameters, we moved to a sorting scenario with mixed material composition (Section 6.2). Here, sorting was simulated with both instantaneous and lagged nozzle activation modes, as described in Section 3.1.3. In doing so, the characteristics of the sorting system were assessed at various belt velocities. Concerning the detection stage, we inferred that no detection errors occur independently of the occupancy density on the belt, which is a valid assumption as experimental investigations with the setup in [37] have shown.

The simulations were run for 5 s physical times, because it was observed that the sorting results did not change more than 1 % for the last second. Thus, the sorter reached a stationary operational mode. A mass flow inlet was used to provide the feed material in a quadratic domain of [0.1, 0.06, 0.23] m. The results of the simulations are plotted separately for the reject (negative, to sort out) and the accept fraction (positive, not to sort out). Bar charts are used to visualize the simulation results, where the blue bars of the reject fraction show the true negative rate (TNR) and the green bars of the accept fraction show the true positive rate (TPR). Both

rates are defined as  $TNR = \frac{True\ negatives}{True\ negatives + False\ positives}$  and  $TPR = \frac{True\ positives}{True\ positives + False\ negatives}$ .

## 6.1 Validation of derived optimal sorting parameters

### 6.1.1 Geometrical parameters

The first simulations were performed with parameters obtained in optimization runs with geometric variables only (optimization O.1). Nozzles were activated permanently to assess if all particles were ejected correctly with the optimized positions and alignments of the sorter components. Consequently, only reject material was considered. Fig. 13 presents the sorting results in bar diagrams. Blue bars indicate correctly separated particles, while yellow bars indicate particles that fell beside the containers. On the left side, we see brick and sand-lime brick sorted at 100  $g/s$ . On the right side, results of sorting at 500  $g/s$  mass flow are shown. From all plots, a high ejection accuracy can be seen for conveyor belt velocities to 2.1  $m/s$ . It decreases slightly for higher belt velocities when particle slip occurs. The largest single decay can be seen in Fig. 13 (c) at 2.9  $m/s$ , where the accuracy is 84 %.

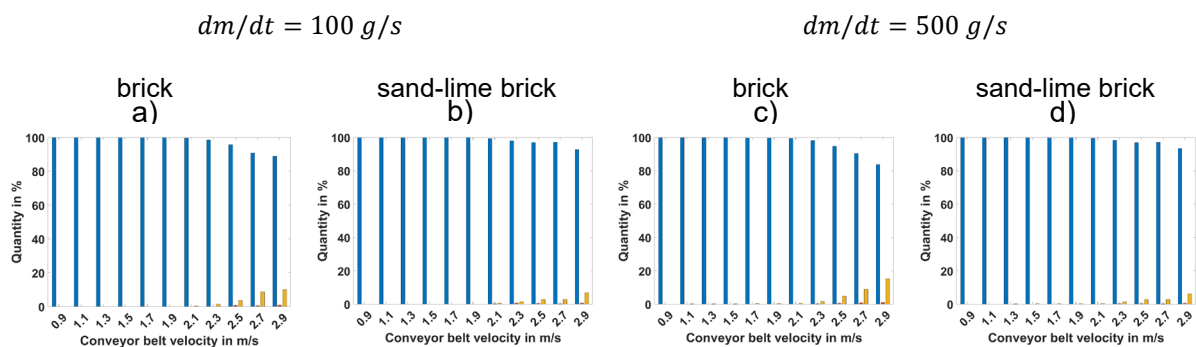
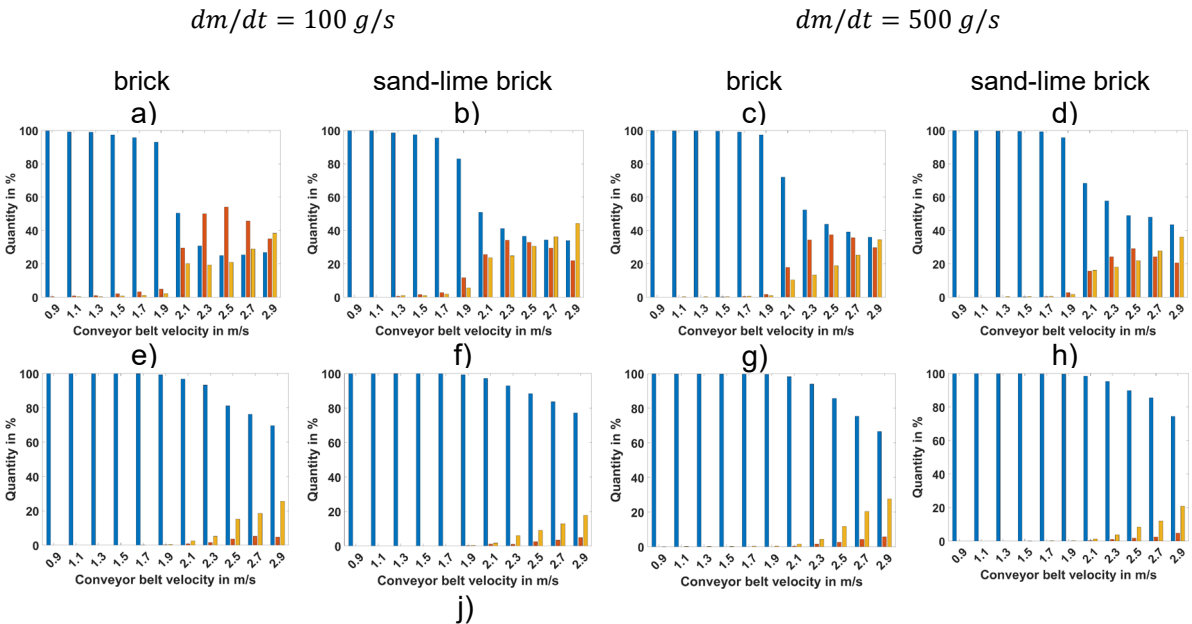


Fig. 13: Correctly separated particles (TNR, blue bars) for a continuously operating nozzle. The yellow bars indicate particles that missed the containers.

### 6.1.2 Temporal parameters

As a next evaluation step, the single component materials were sorted under activation and deactivation of nozzles. For that, the two optimized temporal variables from O.2 were used in this setup. It was tested if the activation duration and activation offset yielded good sorting results for a pure material stream. The three sorting models – line-scan, tracking and ICV – were compared. Again, brick and sand-lime brick were sorted at 100  $g/m$  and 500  $g/m$  each.

Fig. 14 shows all results obtained. The rows show different scenarios sorted with a fixed sorting algorithm; columns compare different sorting algorithms for a fixed scenario (material and mass flow rate). Results of line-scan sorted material are shown in the first row, tracking scenarios are shown in the second row, and ideal sorted scenarios in the last row. Line-scan sorted runs (a-d) show good sorting results for conveyor belt velocities to 1.7 m/s. Here, the TNR decays heavily from around 90 % at 1.9 m/s down to around 30 % at 2.9 m/s. The results show a direct dependence on the particle velocity distribution. Since the line-scan algorithm must assume a fixed particle velocity, which was chosen as the average velocity obtained in Section 4.1, the assumption error grows for a faster belt velocity where slip occurs, and the velocity distribution along the belt broadens. The tracking (e-h) performed significantly better. We can see TNR close to 100 % for conveyor belt velocities to 1.9 m/s at all sorting scenarios. The TNR decays to 70 % for brick and 75 % for sand-lime brick at 2.9 m/s. Lastly, we compare the results to the benchmark algorithm that uses the exact particle velocities to predict nozzle activation (i-l). The results are qualitatively analogous to the tracked sorting but decay slightly less at occurring particle slip on the belt starting at 2.1 m/s. As we would expect, the exact particle velocity differs slightly from the predictions made by the tracking algorithm, leading to 7% – 10 % higher accuracies at 2.9 m/s.





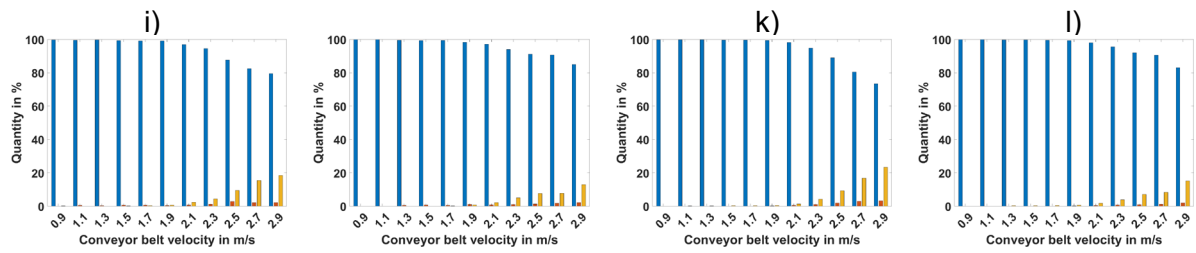


Fig. 14: Correctly separated particles (TNR, blue bars) for (a) – (d) line-scan, camera-based sorting, (e) – (h) area-scan, camera-based sorting, and (i) – (l) ideal sorting for a pulsed operated nozzle. Red bars denote falsely sorted particles (wrong container), and yellow bars denote lost particles (missed both containers).

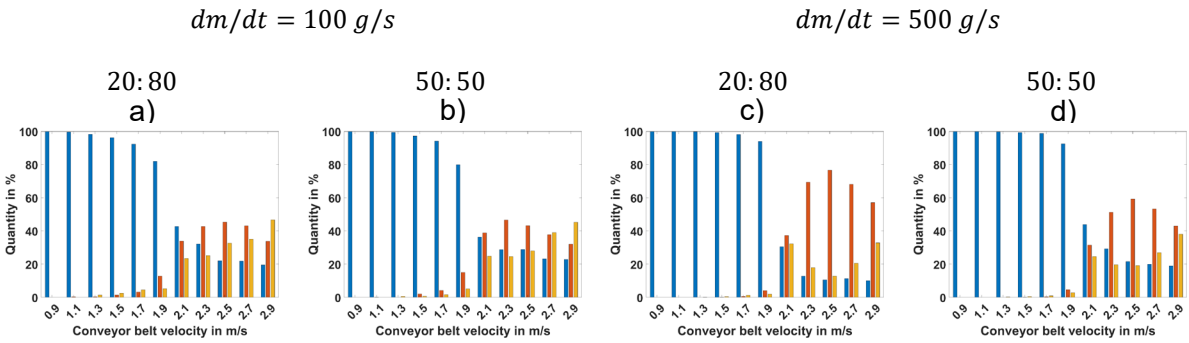
Obviously, the optimized geometric and temporal parameters lead to very robust sorting setups. The sorting setups were successfully adapted to the increased conveyor belt velocities.

## 6.2 Investigation of sorting accuracy of a mixed material

After evaluating the adaption of the sorting setups to changed conveyor belt velocities, the sorting of mixed bulk material at those velocities was investigated. For that, the validated parameters were applied to the model in realistic sorting scenarios in the following. All scenarios were compared for the two nozzle operation modes. Because nozzles have to be activated in short succession at high occupancy densities and fast particle velocities, the reaction time to a triggered activation is crucial. We, therefore, simulated sorting at an instantaneous mode, where the fluid field is present immediately after activation. This corresponds to a fast-sorting system, which is not realizable in reality. It was compared to a lagged operational mode, where nozzle activation and deactivation took an additional 5 ms. That corresponds to a slow sorting system. In the system described in [37], similar lag times were found. In all simulations, sand-lime brick with fractions of 20 % and 50 % was sorted out at mass flows of 100 g/s and 500 g/s.

### 6.2.1 Fast sorting system: Instantaneously activated nozzles

The simulation results with instantaneous nozzle activation are presented in the following. In Fig. 15, the sorting results of the reject fraction (sand-lime brick) are plotted. The percentage of the correctly ejected particles (TNR) is represented by the blue bars. In general, the results are very similar to those of pure material sorting. The TNR of the line-scan sorted scenarios (a-d) deteriorates at 1.7 m/s at 100 g/s and at 1.9 m/s at 500 g/s. The lowest sorting accuracy is achieved in the 20:80 scenario with 500 g/s mass flow at 2.9 m/s with about 10 %. Analogous to the findings in Section 6.1, the line-scan algorithm performed worst as soon as the particle velocity broadened widely due to the slip between the particles and belt. In contrast, the tracking algorithm showed very good sorting precision. Nearly 100 % of reject material was sorted out for velocities up to 1.9 m/s. From here, a slow decline is notable for increasing belt velocities. Interestingly, the lowest TNR is found again at 20: 80 with 500 g/s mass flow. The performance loss in this scenario may be linked to the sorter characteristics that depend on the specific operational point at which the sorter is run. This includes mainly mass flow and material proportions, as experimentally shown in [15]. Concerning the results of ideally sorted scenarios (i-l), only slight differences compared to the tracking results can be detected. The numerical benchmark performed 3 % – 5 % better than the tracking.



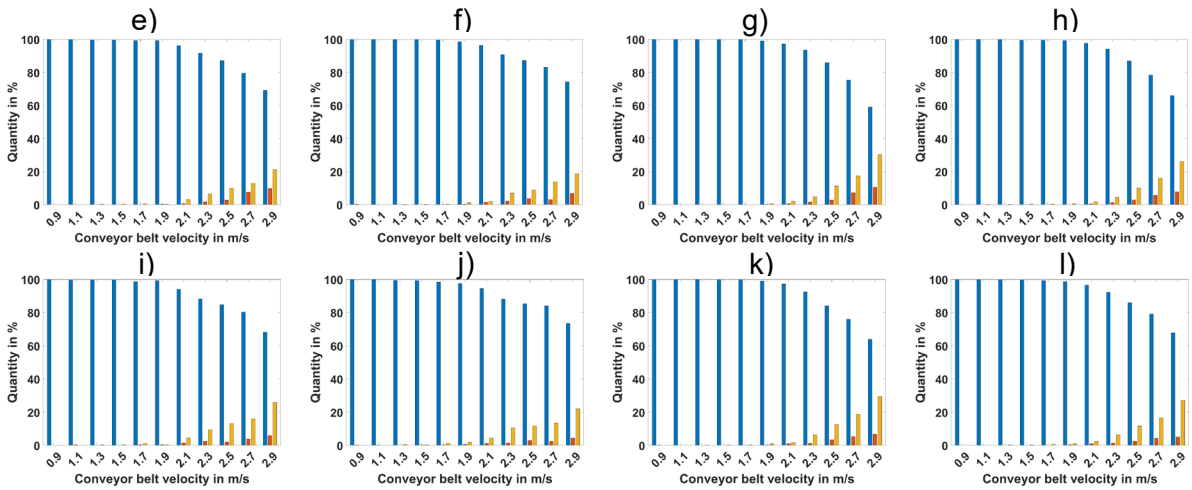


Fig. 15: Correctly separated particles (TNR, blue bars) for (a) – (d) line-scan, camera-based sorting, (e) – (h) area-scan, camera-based sorting, and (i) – (l) ideal sorting for a pulsed operated nozzle without activation or deactivation lag. Red bars denote falsely sorted particles (wrong container), and yellow bars denote lost particles (missed both containers).

Since we considered a mixed material flow, the influence of the sorting stage on the accept fraction should be minimal to yield a pure sorted fraction. An indirect measure for that purity is the already introduced true positive rate (TPR), which is represented by the green bars in Fig. 16. It denotes the percentage of correctly accepted particles. Red bars denote the falsely ejected particles (by-catch), and the yellow bars particles that did not hit any container. Due to the significant similarity of all sorting models, we will focus on the results by tracking Fig. 16 (e) – (h). At a 20:80 mixture with  $100\text{ g/s}$  mass flow, there is no notable change in TPR for belt velocities up to  $2.1\text{ m/s}$ . For faster velocities, the TPR declines sharply. This is due to the particles that did not hit the container. Their number increases proportionally, as the yellow bars indicate. The cause of this increase is the spreading particle velocity at faster belt velocities. The accept container opening could only collect particles whose trajectories deviated less than  $3\text{ cm}$ . As we increased the reject mass flow to  $100\text{ g/s}$ , which is the case at 20:80 for  $500\text{ g/s}$  (comp. Fig. 16 (g)), the TPR increases slightly from  $78\%$  to  $84\%$  from  $0.9\text{ m/s}$  to  $2.1\text{ m/s}$ . The TPR is increased even more in the last sorting scenario (Fig. 16 (h)), where TPR increases from  $53\%$  to  $68\%$  in the same velocity range. However, the gain is

based on a lower TPR level, meaning that the overall purity in this scenario is the lowest. The decreasing rate of falsely ejected particles, indicated by the red bars, implies that these findings are a result of the enlarged purity of the sorting process and cannot be explained by the accept particles that jump beside, since their proportion is nearly constant. Growing sorting purity, expressed as less by-catch, must be caused by enhanced particle singulation on the conveyor belt due to a faster belt velocity. The likely explanation is the decreased occupancy density (comp. Fig. 8 (b)). Since the occupancy density is an indirect measure of particle proximity on the conveyor belt, particle distances in both x- and y-direction increase, and clusters of mixed material are presumably less likely to form. As a result, accept material is falsely ejected less often. Consequently, this effect grows with the count of nozzle activations, which is directly proportional to the reject material mass flow. It is important to state that the increasing TPR comes with no loss in TNR up to 1.9 m/s belt velocity (comp. Fig. 15) and only slight reduce of around 3 % at 2.1 m/s.

These results suggest that increasing the conveyor belt velocity is beneficial until 1.9 m/s. However, instantaneous nozzle activations cannot be realized in real-world sorter applications yet, but increasing valve opening speed is a current field of research [44].

$dm/dt = 100 \text{ g/s}$		$dm/dt = 500 \text{ g/s}$	
20:80	50:50	20:80	50:50

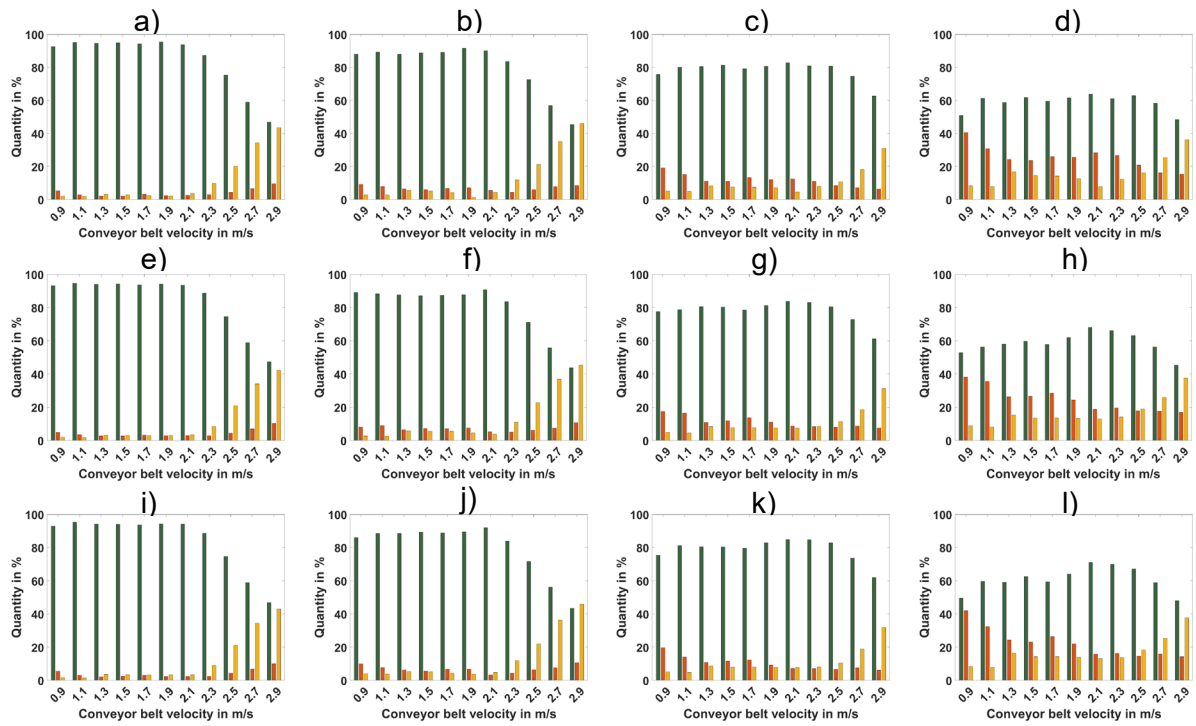


Fig. 16: Correctly not separated particles (TPR, green bars) for (a) – (d) line-scan, camera-based sorting, (e) – (h) area-scan, camera-based sorting, and (i) – (l) ideal sorting for a pulsed operated nozzle without activation or deactivation lag. Red bars denote falsely sorted particles (wrong container), and yellow bars denote lost particles (missed both containers).

## 6.2.2 Realistic sorting system: Lagged activated nozzles

In this simulation series, previous simulations were repeated with a nozzle lag of  $5\text{ ms}$ . In real sorting systems, a lag is always present due to signal processing and mechanical valve opening. The lag becomes important if a nozzle needs to be activated in short succession. If such a situation occurs, a time period of  $10\text{ ms}$  exists, where a reject particle can pass the sorting stage without being deflected, although it was detected (see Fig. 5 and Section 3.1.3 for details).

The results of sorted reject material are presented in Fig. 17. Compared to Fig. 15, the line-scan sorted scenarios (a-d) do not reach 100 % TNR at belt velocities  $0.9 - 1.3\text{ m/s}$ . TNR is around 90 % at  $100\text{ g/s}$  for a 20:80 composition at those velocities. Furthermore, the TNR declines as the reject mass flow increases. At  $0.9\text{ m/s}$  of a 50:50 composition with  $500\text{ g/m}$  (d),

the TNR is 66 %. The decline stems from the aforementioned effect of nozzle blocking, which appeared when two particles followed shortly at the same y-coordinate. This effect is more pronounced at higher mass flows since the possibility of two following particles increases. The exact probability depends on the lateral distribution of reject material on the belt and the reject material mass flow.

The same trend was observed for results sorted by tracking (e-h). Here, the decline of TNR lies around 30 % when increasing the proportions of the reject material (sand-lime brick) at belt velocities up to 2.1 m/s. In contrast to the simulations without delayed nozzles, an increase in belt velocity is followed by a decrease in TNR at nearly all velocities. The performance of the ideal sorting model (i-l) was similar to the tracking sorting model. Sorting by tracking showed to be very robust even at high occupancy densities (~50 %) and fast particle movement, as the comparison between Figs. 17 (h) and (l) shows.

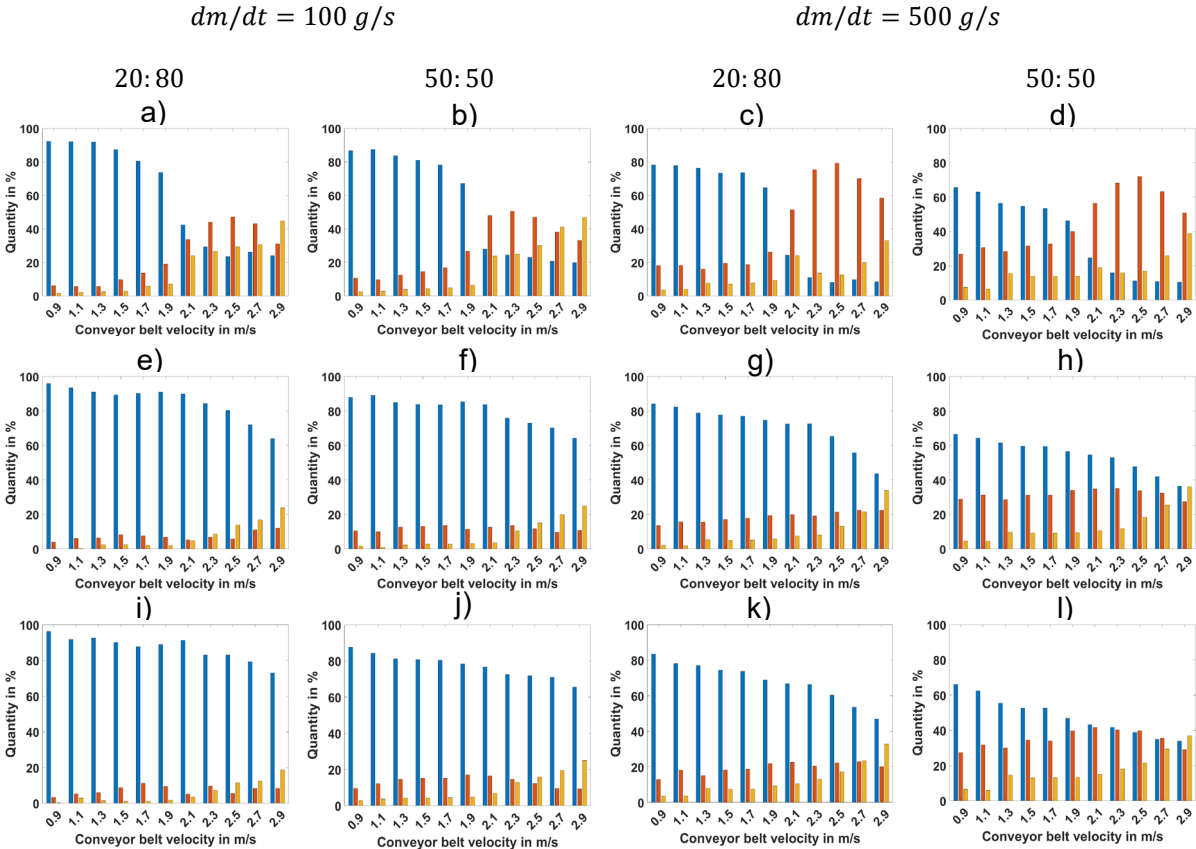
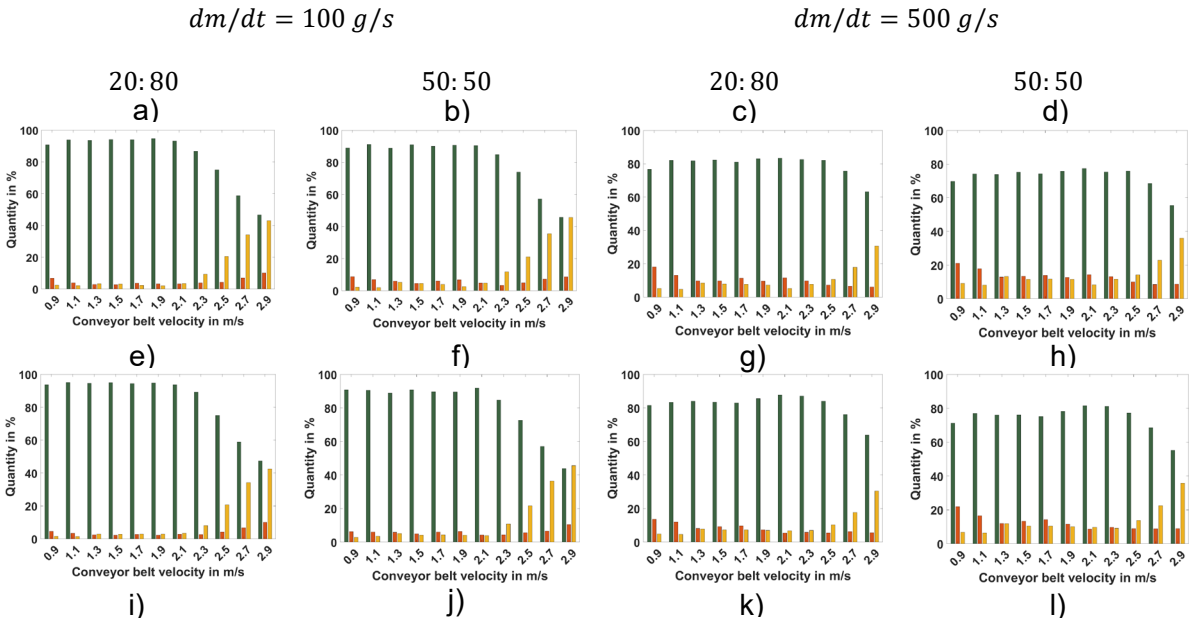


Fig. 17: Correctly separated particles (TNR, blue bars) for (a) – (d) line-scan, camera-based sorting, (e) – (h) area-scan, camera-based sorting, and (i) – (l) ideal sorting for a pulsed operated nozzle with activation and deactivation lag. Red bars denote falsely sorted particles (wrong container), and yellow bars denote lost particles (missed both containers).

Analogous to the findings in the previous Section 6.2.1, the TPRs differ only slightly if different sorting models are used (see Fig. 18). The decay of TPR with an increasing reject fraction mass flow, as it is found in Fig. 16, was gradually less pronounced if nozzles are operated in lagged mode. Additionally, the gain of TPR at increased belt velocities was minor: it is at most 10 % from 0.9 m/s to 2.1 m/s, see Fig. 18 (h).

The increased TPR, if compared to Section 6.2.1, is a result of the delayed nozzle activation, which led to the nozzles being activated less frequently. During the blocked period of 10 ms, no particles were hit. Hence, the by-catch was reduced. This effect became more prominent as the reject mass flow, i.e., the count of activated nozzles, increased. However, there was a trade-off between TNR and TPR if nozzle activation was delayed by 5 ms. An increase in one quantity was connected with a decrease in the other, and vice versa.



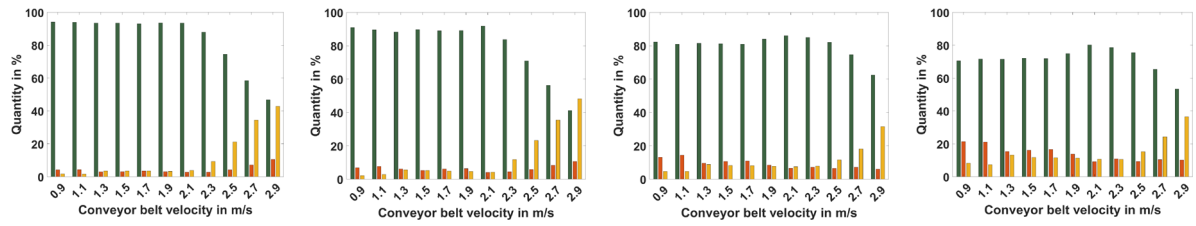


Fig. 18: Correctly not separated particles (TPR, green bars) for (a) – (d) line-scan, camera-based sorting, (e) – (h) area-scan, camera-based sorting, and (i) – (l) ideal sorting for a pulsed operated nozzle with activation and deactivation lag. Red bars denote falsely sorted particles (wrong container), and yellow bars denote lost particles (missed both containers).

To sum up, the results of Section 6.2 show that optimized sorting stages yielded very good sorting outcomes in 3D DEM-CFD simulations. If applied to real sorting systems, the optimization is able to drastically cut the setup time for a sorting plant, as experimental calibration becomes nearly obsolete in terms of sorting stage arrangement. Certain bulk properties, such as particle mass, particle protection area or drag coefficient and details on the nozzle velocity field must be known in advance to apply the approach. Furthermore, it must be known if particles move with belt velocity or a velocity is differing from it. The configuration of the sorting setup is based on the particle velocity. Having discussed the application of optimized sorting parameters to the DEM-CFD and the simulation results, the final Section 6.2.3 of this paper addresses the nozzle activation in further detail.

### 6.2.3 Analysis of nozzle activation

To gain further insight into the reasons for deviating sorting results between instantaneous and lagged operational mode, some analysis of nozzle data was conducted. In particular, the occurrence of the scenarios depicted in Fig. 5 was analyzed. The data was taken from simulations that were performed with the tracking algorithm at 1.1  $m/s$  belt velocity. For simplification, the four simulated scenarios are expressed in terms of the mass flow of reject material. The four mass flows correspond to the four scenarios shown in the columns of Fig.



15 - Fig. 18, respectively. A mixture of 20:80 at 100  $g/s$  mass flow corresponds to a reject material mass flow of 20  $g/s$ , a mixture of 50:50 at 100  $g/s$  to 50  $g/s$  and so on. Fig. 19 (a) shows the count of nozzle activations for all reject material mass flows and both operational modes plotted against the simulation time. This corresponds to the scenarios (a) and (d) in Fig. 5. As the mass flow is increased, the deviation between both modes grows: While there is no significant difference at 20  $g/s$ , nozzles are activated 25 % more often in instantaneous mode at 250  $g/s$  after 5 s. The frequency of a nozzle being fully blocked clearly depends on the mass flow of material to be sorted out.

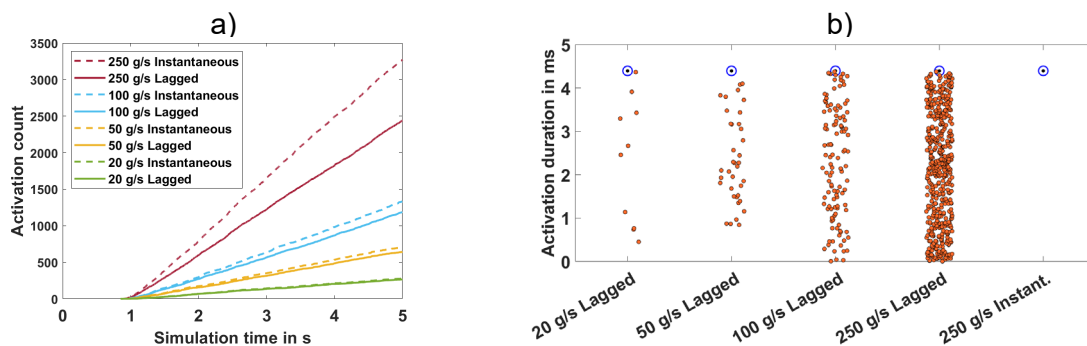


Fig. 19: Nozzle activation count of instantaneous and lagged operated sorting (a) and nozzle activation durations  $\Delta t$  in lagged operated simulations compared with a simulation in instantaneous activation mode (b). Blue dots represent the set activation duration, and orange dots denote reduced activation durations. Nozzle data is evaluated for simulations sorted by tracking at 1.1  $m/s$  belt velocity and plotted for all reject fraction mass flows.

In Fig. 19 (b), the distribution of nozzle activation duration  $\Delta t$  is presented for all mass flows in lagged mode. For comparison with instantaneous nozzle activation, it is also shown at 250  $g/s$ . The set activation duration of 4.4  $ms$ , which was obtained by optimization as shown in Fig. 12 (a), is denoted by the blue dots. Deviating values, i.e., reductions of the ejection window, are presented as orange dots. In other words, each orange dot stands for a narrowed activation window, as illustrated in scenario (c) in Fig. 5. As expected, the number of reduced activation windows increased at higher reject fraction mass flows. Activation windows were narrowed 10

times at 20 *g/s* and 441 times at 250 *g/s*, which correspond to 4 % and 18 % of the total activations, respectively. The narrowing was distributed equally between 0 and the set activation duration of 4.4 *ms*. In the case of instantaneously activated nozzles, no narrowing occurred.

In summary, the findings showed that nozzle characteristics influenced the overall sorting performance drastically. Due to the time lag between signal processing and the actual formation of the fluid jet, two negative effects followed: Either the time window of activation was either narrowed, or a controlled nozzle was not activated at all. Both phenomena contributed to a lowered sorting accuracy, while decreasing the by-catch, as observed in Section 6.2.2. However, not all narrowed activation windows resulted in a reject particle being falsely sorted. This depended on several factors of the complex particle-fluid interaction and was studied thoroughly in [44]. Those factors are, for example, the particle shape, the particle orientation and the exact location of fluid drag on the particle surface. In any case, the speed of nozzle activation was the crucial limitation of the analyzed sorting system. Faster nozzles were able to handle higher mass flows of material to be sorted out at higher conveyor belt velocities.

## **7 Conclusions**

We proposed a method to compute optimal sorting setups in terms of geometrical and temporal parameters for optical belt sorters operated at arbitrary conveyor belt velocities. As a result, fast computation of sorting stage arrangement for an adaption to changing conveyor belt velocities was feasible. The method takes advantage of calmed particles, which allows a reduction to a 2D problem, which then can be optimized. Optimized parameters, namely reject container and nozzle orientation and position as well as nozzle activation time and activation offset, were numerically validated in 3D DEM-CFD simulations with a non-spherical shaped bulk material consisting of brick and sand-lime brick. The main findings and possible next steps can be summarized as follows:

- As long as no major particle slip occurred, the optimized sorting parameters yielded excellent sorting results at increased conveyor belt velocities.
- A change in the conveyor belt velocity influenced the occupancy density on the conveyor belt, increasing the sorting accuracy through the reduction of by-catch.
- The increase in accuracy was more pronounced with instantaneously activated nozzles than with lagged activated nozzles. For lagged activation, this was dependent on the reject material mass flow, since nozzle valve opening and closing in short succession occurred more often.
- The proposed approach of adapting the sorting components is useful if the goal is to reduce conveyor belt occupancy or by-catch.
- To address slip and the broadening of particle velocity, a different conveyor belt material may be used to increase the friction at higher belt velocities.
- The next step to improve sorting performance and save costs for compressed air is to calculate individual activation durations for each particle. Such an approach can account for uncertainties in particle position measurements of real camera systems.

## **Acknowledgements**

The IGF project 20354 N of the research association Forschungs-Gesellschaft Verfahrenstechnik e.V. (GVT) is supported by the AiF in a program to promote the Industrial Community research and Development (IGF) by the Federal Ministry of Economic Affairs and Climate Action on the basis of a decision of the German Bundestag. Computing resources were partially funded by the Deutsche Forschungsgemeinschaft (DFG, German Research Foundation) – Project-ID 463921749.

## **List of Symbols**

### **Latin letters**

$A$  [m<sup>2</sup>] projection area

$c$	[-]	coefficient
$d$	[m]	diameter
$\vec{F}$	[N]	force vector
$J$	[kg m <sup>2</sup> ]	mass inertia tensor
$k$	[N m <sup>-1</sup> ]	spring stiffness
$l$	[m]	length
$m$	[kg]	mass
$\vec{n}$	[-]	normal vector
$n$	[-]	particle number
$p$	[N m <sup>-2</sup> ]	pressure
$r$	[m]	radius
$R$	[m]	radius
$Re$	[-]	Reynolds number
$\vec{T}$	[N m]	torque vector
$t$	[s]	time
$\vec{t}$	[-]	tangential vector
$\vec{u}$	[m s <sup>-1</sup> ]	velocity vector
$\vec{v}$	[m s <sup>-1</sup> ]	velocity vector
$\vec{x}$	[m]	particle position vector
$w$	[-]	summand weight

### Greek letters

$\gamma$	[kg s <sup>-1</sup> ]	damping coefficient
$\delta$	[m]	overlap
$\Delta\alpha$	[°]	nozzle rotation
$\Delta\beta$	[°]	reject container rotation
$\Delta t$	[s]	nozzle activation duration
$\Delta x$	[m]	displacement
$\varepsilon$	[-]	local voidage
$\eta$	[N s m <sup>-2</sup> ]	dynamic fluid viscosity
$\Lambda_i^{-1}$	[-]	rotation matrix
$\mu$	[-]	friction coefficient

$\vec{\xi}$	[m]	displacement vector
$\rho$	[kg m <sup>-3</sup> ]	density
$\tau$	[N m <sup>-2</sup> ]	stress tensor
$\tau$	[s]	nozzle activation offset
$\phi$	[-]	sphericity
$\chi$	[-]	correction factor
$\vec{\omega}$	[s <sup>-1</sup> ]	angular velocity vector

### Sub- and Superscripts

$C$	Coulomb
$c$	contact
$c$	reject container
$D$	drag
$e$	effective
$E$	fluid field edge
$f$	fluid
$g$	gravitation
$i$	initial value
$i$	particle index
$n$	normal
$n$	nozzle
$p$	particle
$p$	pressure
$r$	rolling
$rel$	relative
$t$	tangential
$\cdot$	temporal derivation
$\perp$	perpendicular to flow direction

### Abbreviations

B	brick
CB	conveyor belt material

CFD	computational fluid dynamics
COR	coefficient of restitution
DEM	discrete element method
SB	sand-lime brick
SW	sorter wall material
TNR	true negative rate
TPR	true positive rate

## References

- [1] M. Ploschner, T. Čížmár, M. Mazilu, A. Di Falco, and K. Dholakia, “Bidirectional Optical Sorting of Gold Nanoparticles,” *Nano Lett.*, vol. 12, no. 4, pp. 1923–1927, Apr. 2012, doi: 10.1021/nl204378r.
- [2] F. Brandt and R. Haus, “New concepts for lithium minerals processing,” *Minerals Engineering*, vol. 23, no. 8, pp. 659–661, Jul. 2010, doi: 10.1016/j.mineng.2010.03.021.
- [3] M. Dehler, “Optical Sorting of Ceramic Raw Material,” *Tile & Brick Int.*, vol. 19, p. 4, 2003.
- [4] R. P. Haff, T. C. Pearson, and E. Maghirang, “A multispectral sorting device for isolating single wheat kernels with high protein content,” *Food Measure*, vol. 7, no. 4, pp. 149–157, Dec. 2013, doi: 10.1007/s11694-013-9150-7.
- [5] J. R. Mathiassen, E. Misimi, M. Bondø, E. Veliyulin, and S. O. Østvik, “Trends in application of imaging technologies to inspection of fish and fish products,” *Trends in Food Science & Technology*, vol. 22, no. 6, pp. 257–275, Jun. 2011, doi: 10.1016/j.tifs.2011.03.006.
- [6] L. A. Paluchowski, E. Misimi, L. Grimsmo, and L. L. Randeberg, “Towards automated sorting of Atlantic cod (*Gadus morhua*) roe, milt, and liver – Spectral characterization and classification using visible and near-infrared hyperspectral imaging,” *Food Control*, vol. 62, pp. 337–345, Apr. 2016, doi: 10.1016/j.foodcont.2015.11.004.

- [7] Y. J. Heo, S. J. Kim, D. Kim, K. Lee, and W. K. Chung, "Super-High-Purity Seed Sorter Using Low-Latency Image-Recognition Based on Deep Learning," *IEEE Robot. Autom. Lett.*, vol. 3, no. 4, pp. 3035–3042, Oct. 2018, doi: 10.1109/LRA.2018.2849513.
- [8] Bruce, P. Lestringant, Brenneman, Heymann, and A. Oberholster, "The Impact of Optical Berry Sorting on Red Wine Composition and Sensory Properties," *Foods*, vol. 10, no. 2, p. 402, 2021, doi: 10.3390/foods10020402.
- [9] S. P. Gundupalli, S. Hait, and A. Thakur, "A review on automated sorting of source-separated municipal solid waste for recycling," *Waste Manage.*, vol. 60, pp. 56–74, Feb. 2017, doi: 10.1016/j.wasman.2016.09.015.
- [10] N. Dias, N. Belo, A. Máximo, and M. T. Carvalho, "Recovery of glass contained in the heavy residual fraction of Portuguese mechanical Biological Treatment Plants," *Journal of Cleaner Production*, vol. 79, pp. 271–275, Sep. 2014, doi: 10.1016/j.jclepro.2014.05.028.
- [11] M. A. Zulkifley, M. M. Mustafa, A. Hussain, A. Mustapha, and S. Ramli, "Robust Identification of Polyethylene Terephthalate (PET) Plastics through Bayesian Decision," *PLoS ONE*, vol. 9, no. 12, p. e114518, Dec. 2014, doi: 10.1371/journal.pone.0114518.
- [12] E. Scavino, D. A. Wahab, A. Hussain, H. Basri, and M. M. Mustafa, "Application of automated image analysis to the identification and extraction of recyclable plastic bottles," *J. Zhejiang Univ. Sci. A*, vol. 10, no. 6, pp. 794–799, Jun. 2009, doi: 10.1631/jzus.A0820788.
- [13] Robben and Wotruba, "Sensor-Based Ore Sorting Technology in Mining—Past, Present and Future," *Minerals*, vol. 9, no. 9, p. 523, Aug. 2019, doi: 10.3390/min9090523.
- [14] "Directive 2008/98/EC of the European Parliament and of the Council of 19 November 2008 on waste and repealing certain Directives (Text with EEA relevance)." Accessed: Jan. 18, 2022. [Online]. Available: <http://data.europa.eu/eli/dir/2008/98/2018-07-05>
- [15] B. Küppers, I. Seidler, G. R. Koinig, R. Pomberger, and D. Vollprecht, "INFLUENCE OF THROUGHPUT RATE AND INPUT COMPOSITION ON SENSOR-BASED SORTING EFFICIENCY," *Detritus*, no. 9, pp. 59–67, Feb. 2020, doi: 10.31025/2611-4135/2020.13906.

- [16] R. S. Fitzpatrick, H. J. Glass, and R. D. Pascoe, "CFD–DEM modelling of particle ejection by a sensor-based automated sorter," *Miner. Eng.*, vol. 79, pp. 176–184, Aug. 2015, doi: 10.1016/j.mineng.2015.06.009.
- [17] R. D. Pascoe, R. Fitzpatrick, and J. R. Garratt, "Prediction of automated sorter performance utilising a Monte Carlo simulation of feed characteristics," *Miner. Eng.*, vol. 72, pp. 101–107, Mar. 2015, doi: 10.1016/j.mineng.2014.12.026.
- [18] C. Pieper *et al.*, "Numerical modeling of an automated optical belt sorter using the Discrete Element Method," *Powder Technol.*, vol. 301, pp. 805–814, Nov. 2016, doi: 10.1016/j.powtec.2016.07.018.
- [19] C. Pieper *et al.*, "Numerical modelling of an optical belt sorter using a DEM–CFD approach coupled with particle tracking and comparison with experiments," *Powder Technol.*, vol. 340, pp. 181–193, Dec. 2018, doi: 10.1016/j.powtec.2018.09.003.
- [20] B. Doroszuk and R. Król, "ANALYSIS OF CONVEYOR BELT WEAR CAUSED BY MATERIAL ACCELERATION IN TRANSFER STATIONS," *Min. Sci.*, vol. 26, pp. 189–201, 2019, doi: 10.5277/msc192615.
- [21] M. J. Cordero and L. A. Pugnali, "Dynamic transition in conveyor belt driven granular flow," *Powder Technology*, vol. 272, pp. 290–294, Mar. 2015, doi: 10.1016/j.powtec.2014.12.017.
- [22] D. Ilic and C. Wheeler, "Measurement and simulation of the bulk solid load on a conveyor belt during transportation," *Powder Technology*, vol. 307, pp. 190–202, Feb. 2017, doi: 10.1016/j.powtec.2016.11.020.
- [23] S. Kuang, M. Zhou, and A. Yu, "CFD-DEM modelling and simulation of pneumatic conveying: A review," *Powder Technology*, vol. 365, pp. 186–207, Apr. 2020, doi: 10.1016/j.powtec.2019.02.011.
- [24] K. Vollmari, "Experimental and Numerical Analysis of Non-Spherical Particles in Fluidized Process/Energy Technology Systems," p. 177.



- [25] Z. Hu, H. Zeng, Y. Ge, W. Wang, and J. Wang, "Simulation and Experiment of Gas-Solid Flow in a Safflower Sorting Device Based on the CFD-DEM Coupling Method," *Processes*, vol. 9, no. 7, p. 1239, Jul. 2021, doi: 10.3390/pr9071239.
- [26] P. Yin, Y. Hou, and X. Wu, "Simulation of particles screening in pulsating negative pressure shale shaker by coupling CFD and DEM," *EC*, vol. ahead-of-print, no. ahead-of-print, Nov. 2021, doi: 10.1108/EC-12-2020-0737.
- [27] S. T. W. Kuruneru *et al.*, "A Comparative Study of Mixed Resolved–Unresolved CFD-DEM and Unresolved CFD-DEM Methods for the Solution of Particle-Laden Liquid Flows," *Arch Computat Methods Eng*, vol. 26, no. 4, pp. 1239–1254, Sep. 2019, doi: 10.1007/s11831-018-9282-3.
- [28] P. Kieckhefen, S. Pietsch, M. Dosta, and S. Heinrich, "Possibilities and Limits of Computational Fluid Dynamics–Discrete Element Method Simulations in Process Engineering: A Review of Recent Advancements and Future Trends," *Annu. Rev. Chem. Biomol. Eng.*, vol. 11, no. 1, pp. 397–422, Jun. 2020, doi: 10.1146/annurev-chembioeng-110519-075414.
- [29] J. Schäfer, S. Dippel, and D. Wolf, "Force Schemes in Simulations of Granular Materials.," *J. Phys.*, pp. 5–20, 1996, doi: 10.1051/jp1:1996129.
- [30] Y. C. Zhou, B. D. Wright, R. Y. Yang, B. H. Xu, and A. B. Yu, "Rolling friction in the dynamic simulation of sandpile formation," *Physica A: Statistical Mechanics and its Applications*, vol. 269, no. 2–4, pp. 536–553, Jul. 1999, doi: 10.1016/S0378-4371(99)00183-1.
- [31] R. Di Felice, "The voidage function for fluid-particle interaction systems," *Int. J. Multiphase Flow*, vol. 20, no. 1, pp. 153–159, Feb. 1994, doi: 10.1016/0301-9322(94)90011-6.
- [32] A. Hölzer and M. Sommerfeld, "New simple correlation formula for the drag coefficient of non-spherical particles," *Powder Technol.*, vol. 184, no. 3, pp. 361–365, 2008, doi: 10.1016/j.powtec.2007.08.021.
- [33] A. Bauer *et al.*, "Benchmarking a DEM-CFD Model of an Optical Belt Sorter by Experimental Comparison" [Manuscript under review in *CIT (Chemie Ingenieur Technik)*], 2022.

- [34] Wilcox, David C, *Turbulence Modeling for CFD*, Third Edition. La Canada, California: DCW Industries, 2006.
- [35] X. Zheng, X. Jian, J. Wei, and D. Wenzheng, "Numerical and Experimental Investigation of Near-Field Mixing in Parallel Dual Round Jets," *International Journal of Aerospace Engineering*, vol. 2016, pp. 1–12, 2016, doi: 10.1155/2016/7935101.
- [36] R. Naseri Oskouie, M. F. Tachie, and B.-C. Wang, "Effect of Nozzle Spacing on Turbulent Interaction of Low-Aspect-Ratio Twin Rectangular Jets," *Flow Turbulence Combust*, vol. 103, no. 2, pp. 323–344, Aug. 2019, doi: 10.1007/s10494-019-00023-1.
- [37] J. Ludwig *et al.*, "Systematic Determination of the Influence of Factors Relevant to Operating Costs of Sensor-based Sorting Systems," presented at the SBSC 2022.
- [38] H. Wotruba and C. Robben, "Sensor-based ore sorting in 2020," *at - Automatisierungstechnik*, vol. 68, no. 4, pp. 231–238, Apr. 2020, doi: 10.1515/auto-2019-0060.
- [39] G. Maier *et al.*, "Experimental Evaluation of a Novel Sensor-Based Sorting Approach Featuring Predictive Real-Time Multiobject Tracking," *IEEE Trans. Ind. Electron.*, vol. 68, no. 2, pp. 1548–1559, Feb. 2021, doi: 10.1109/TIE.2020.2970643.
- [40] F. Pfaff *et al.*, "TrackSort: Predictive Tracking for Sorting Uncooperative Bulk Materials," San Diego, California, USA, Sep. 2015.
- [41] F. Pfaff *et al.*, "Simulation-Based Evaluation of Predictive Tracking for Sorting Bulk Materials," Baden-Baden, Germany, Sep. 2016.
- [42] G. Maier *et al.*, "Real-Time Multitarget Tracking for Sensor-Based Sorting," *Journal of Real-Time Image Processing*, 2017.
- [43] G. Maier *et al.*, "Motion-Based Material Characterization in Sensor-Based Sorting," *tm - Technisches Messen, De Gruyter*, Oct. 2017, doi: 10.1515/teme-2017-0063.
- [44] A. Leonhard, *Untersuchungen zum pneumatischen Sortieren von Schüttgütern mittels Freistrahlen*. Aachen: Shaker, 2011.

- [45] X. Garcia, J.-P. Latham, J. Xiang, and J. P. Harrison, "A clustered overlapping sphere algorithm to represent real particles in discrete element modelling," *Géotechnique*, vol. 59, no. 9, pp. 779–784, Nov. 2009, doi: 10.1680/geot.8.T.037.
- [46] F. Elskamp, H. Kruggel-Emden, M. Hennig, and U. Teipel, "A strategy to determine DEM parameters for spherical and non-spherical particles," *Granular Matter*, vol. 19, no. 3, p. 46, Aug. 2017, doi: 10.1007/s10035-017-0710-0.
- [47] D. Höhner, S. Wirtz, and V. Scherer, "Experimental and numerical investigation on the influence of particle shape and shape approximation on hopper discharge using the discrete element method," *Powder Technology*, vol. 235, pp. 614–627, Feb. 2013, doi: 10.1016/j.powtec.2012.11.004.
- [48] D. B. Hastie and P. W. Wypych, "Conveyor belt trajectories - comparing predicted to experimental results," pp. 438–445, 2010.
- [49] "MATLAB Documentation." Jan. 19, 2022. [Online]. Available: <https://de.mathworks.com/help/gads/how-the-genetic-algorithm-works.html>
- [50] H.-G. Matuttis and J. Chen, *Understanding the Discrete Element Method Simulation of Non-Spherical Particles for Granular and Multi-body Systems*, 1. Edition. Wiley, 2014.
- [51] Thomas Roessler, Christian Richter, André Katterfeld, and Frank Will, "Development of a standard calibration procedure for the DEM parameters of cohesionless bulk materials – part I: Solving the problem of ambiguous parameter combinations," *Powder Technol.*, vol. 343, pp. 803–812, 2018, doi: <https://doi.org/10.1016/j.powtec.2018.11.034>.
- [52] H. Tang, R. Song, Y. Dong, and X. Song, "Measurement of Restitution and Friction Coefficients for Granular Particles and Discrete Element Simulation for the Tests of Glass Beads," *Materials*, vol. 12, no. 19, p. 3170, Sep. 2019, doi: 10.3390/ma12193170.

## **Appendix A: Calibration of DEM contact parameters**

The calibration of DEM parameters was performed partly adapting the procedure of [46]. We start with the experiment that is influenced by the least number of contact parameters, which leads to the following order with the initial values given in braces.

- 1) Static angle of repose. Mainly influenced by particle – particle (pp) friction (0.5) and pp rolling friction (0.01)
- 2) Dynamic angle of repose: Influenced by pp and particle – wall (pw) contacts. PP parameters are taken from the preceding experiment, pw friction (0.3) and pw rolling friction ( $5e-3$ ).
- 3) Plate impact experiment. Friction parameters play a role; major impact is given by coefficient of restitution (COR) of pp (0.3) and pw (0.2) contacts.
- 4) As a verification step, simulation runs 1) and 2) are repeated with all calibrated parameters to ensure agreement with the experiments.

### **A.1 Static angle of repose**

The static angle of the repose experiment is a standard investigation (see [50], [51]) to determine mechanical friction quantities of bulks. A bulk sample is filled into an open cylinder, which is then slowly pulled up. The filled material falls out and forms a characteristic pile with a corresponding angle of repose that depends on the material friction. To exclude the influence of pw parameters as well as COR, a sensitivity study was conducted as the first step, whereby pw friction parameters and COR were varied in a vast range. As expected, the static angle of the repose experiment showed to be not responsive to those quantities. Simulations with different parameter sets were run until the formed pile angles (Fig. A-1 right) agreed with the experiments (Fig. A-1 left). The resulting angles and quantity ranges are shown in Tab. A-1. Since friction also occurs at the plate impact (see Section A.3), final values can only be determined by the last experiment and must be validated again (see Section A.4).

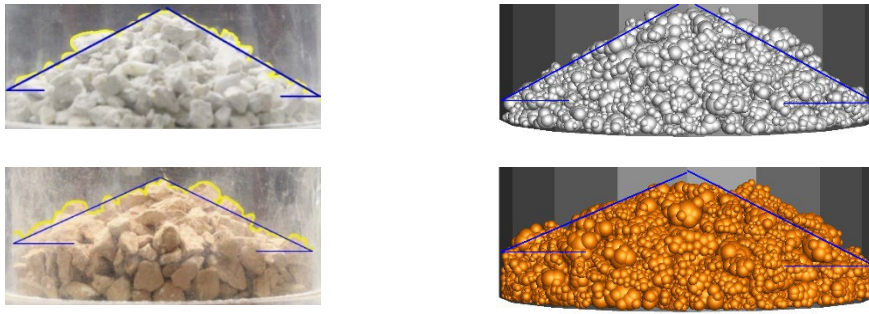


Fig. A-1: Static angle of repose of both materials in experiment and simulation.

Material	Experiment [°]	Simulation [°]	Sliding friction	Rolling friction
			P-P [-]	P-P [-]
Sand-lime brick	29.0	30.7	0.13-0.20	$2 \cdot 10^{-2}$
Brick	24.2	24.3	0.15-0.22	$5.8 \cdot 10^{-3}$

Tab. A-1: Static angles of repose and determined contact parameters (sliding and rolling friction) for both materials.

## A.2 Dynamic angle of repose

The next set of contact parameters is calibrated by measuring the dynamic angle of repose. Here, a drum was filled by 30 %, and the dynamic angle of repose was measured at three different rotation velocities, i.e., 10, 15 and 20 rotations per minute. Experiments were repeated 10 times for each configuration. Two different wall materials were used. To account for both wall materials, the drum interior was glued with conveyor belt rubber in a second step after investigating the sorter wall material (steel). Significant differences between the two wall materials were, however, not detected. Exemplary results on the dynamic angle of repose are shown in Fig. A-2 for both sand-lime brick and brick as obtained in the experiment and simulation for steel as wall material. The measured angles and friction parameters are summarized in Tab. A-2.

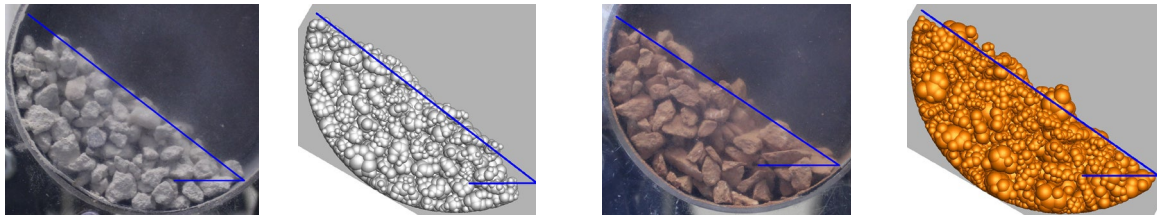


Fig. A-2: Dynamic angle of repose of both materials in experiment and simulation, 10 rotations per minute for steel as wall material.

Material	Experiment [°]			Simulation [°]			Sliding friction P-SW and P-CB [-], Rolling friction P-SW and P-CB [-]
	10 rpm	15 rpm	20 rpm	10 rpm	15 rpm	20 rpm	
Sand-lime brick	35.9	36.6	36.7	34.0	35.7	38.2	0.50, $7.5 \cdot 10^{-3}$
Brick	37.0	35.7	36.3	35.3,	34.0	38.7	0.67, $5.8 \cdot 10^{-3}$

Tab. A-2: Dynamic angles of repose and determined contact parameters (sliding and rolling friction) for both materials. (P) refers to either sand-lime brick or brick, (CB) to the conveyor belt and (SW) to the sorter wall material.

### A.3 Plate impact investigation

To determine coefficients of restitution for particle-particle and particle-wall contacts, a plate impact experiment was conducted (see Fig. A-3 a). The experiments were run by dropping 200 g of material onto a 45° inclined plate, on which the contact material of interest was fixed, namely particles or wall material. Dropped material was collected in three containers (m1 – m3) and weighted for each container (see Fig. A-3 b). The experiments were repeated 10 times. This approach was chosen due to the highly irregular-shaped particles that do not allow for a precise measurement of the COR in a single contact scenario, as it is common for spheres [52].

a)

b)

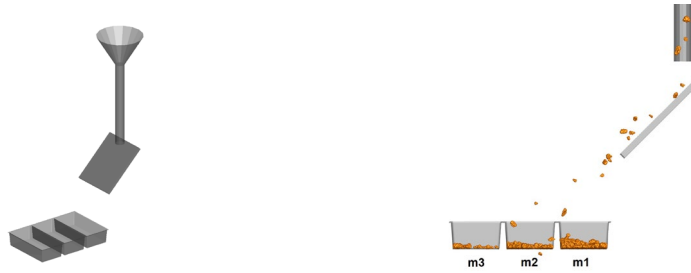


Fig. A-3: Plate impact experiment setup (a) and simulated drop of brick on sorter wall material (b).

Calibration was performed with respect to mass proportions in the first two boxes, m1 and m2, because masses in m3 were too small and fluctuating. CORs were varied, as were the friction parameters, because sliding also occurred between contact partners. Due to the short contact time of the particles in the experiment, rolling friction is neglected as a parameter.

Tab. A-3 sums up mass proportions as well as coefficients of restitution (COR) and sliding friction coefficients as obtained as best fit in the simulations. Note that conveyor belt and sorter wall material did not differ significantly in terms of the obtained mass proportion. Therefore, both materials are associated with the same COR and sliding friction values.

Material	Experiment (P-CB and P-SW)	Experiment (P-SB)	Experiment (P-B)	Simulation (P-CB, P-SW), COR, sliding friction		Simulation, (P-SB), COR, sliding friction		Simulation, (P-B), COR, sliding friction	
Sand-lime brick	1.54	1.62	1.47	1.54, 0.19, 0.45	1.63, 0.19, 0.17	1.47, 0.215, 0.16			
Brick	1.58	1.86	1.5	1.59, 0.1, 0.6	1.8, 0.215, 0.165	1.5, 0.24, 0.14			

Tab. A-3: Mass proportions  $m_1/m_2$  of plate impact and determined contact parameters (COR, sliding friction) for both materials. (P) refers to either sand-lime brick or brick, (SB) to sand-lime brick, (B) to brick, (CB) to the conveyor belt and (SW) to the sorter wall material.

#### **A.4 Verification of DEM contact parameters**

To verify all determined simulation parameters, simulations for static and dynamic angle of repose were repeated with altered sliding friction parameters and COR calibrated with the plate impact experiment. In the validation simulations, we observed that slight changes in friction parameters that were made for plate impact calibration in addition to the adjusted values for COR (details on this investigation not given) still resulted in angles within the range of angle of repose experiments (Sections A.1 and A.2). As a result, we have successfully calibrated our material model. The final calibrated parameters are given in Tab. 1 in the main section of the manuscript.